

Plasma turbulence generated in a 3D current sheet with magnetic islands

Valentina Zharkova^{1,*}, Qian Xia²

¹Department of Mathematics, Physics and Electrical Engineering, Northumbria University, Newcastle, NE1 8ST, UK ; ² Culham Centre for Fusion Energy, Abingdon, OX14 3DB, UK

Correspondence*:
Valentina Zharkova
valentina.zharkova@northumbria.ac.uk

2 ABSTRACT

3 In this paper we aim to investigate the kinetic turbulence in a reconnecting current sheet (RCS)
4 with X- and O-nullpoints and to explore its link to the features of accelerated particles. We carry
5 out simulations of magnetic reconnection in a thin current sheet with 3D magnetic field topology
6 affected by tearing instability until the formation of two large magnetic islands using particle-
7 in-cell (PIC) approach. The model utilises a strong guiding field that leads to separation of the
8 particles of opposite charges, generation of a strong polarisation electric field across the RCS and
9 suppression of kink instability in the 'out-of-plane' direction. The accelerated particles of the same
10 charge entering an RCS from the opposite edges are shown accelerated to different energies
11 forming the 'bump-in-tail' velocity distributions that, in turn, can generate plasma turbulence in
12 different locations. The turbulence-generated waves produced by either electron or proton beams
13 can be identified from the energy spectra of electromagnetic field fluctuations in the phase and
14 frequency domains. From the phase space analysis we gather that the kinetic turbulence may
15 be generated by accelerated particle beams, which are later found to evolve into a phase-space
16 hole indicating the beam breakage. This happens at some distance from the particle entrance
17 into an RCS, e.g. about $7d_i$ (ion inertial depth) for the electron beam and $12d_i$ for the proton
18 beam. In a wavenumber space the spectral index of the power spectrum of the turbulent magnetic
19 field near the ion inertial length is found to be -2.7 that is consistent with other estimations.
20 The collective turbulence power spectra are consistent with the high-frequency fluctuations of
21 perpendicular electric field, or upper hybrid waves, to occur in a vicinity of X-nullpoints, where the
22 Langmuir (LW) can be generated by accelerated electrons with high growth rates, while further
23 from X-nullpoints or on the edges of magnetic islands, where electrons become ejected and
24 start moving across the magnetic field lines, Bernstein waves can be generated. The frequency
25 spectra of high and low-frequency waves are explored in the kinetic turbulence in parallel and
26 perpendicular directions to the local magnetic field showing noticeable lower hybrid turbulence
27 occurring between the electron's gyro- and plasma frequencies seen also in the wavelet spectra.
28 Fluctuation of the perpendicular electric field component of turbulence can be consistent with the
29 oblique whistler waves generated on the ambient density fluctuations by intense electron beams.
30 This study brings attention to a key role of particle acceleration in generation kinetic turbulence
31 inside current sheets.

32

33 **Keywords:** particle acceleration, magnetic reconnection, solar wind, plasma, methods: numerical

1 INTRODUCTION

34 The processes of magnetic reconnection are often observed during eruptive events in the Sun (flares and
 35 coronal mass ejections (CMEs)) (Antiochos et al., 1994; Antiochos, 1998; Zharkova et al., 2011; Vilmer
 36 et al., 2011; Benz, 2017), heliospheric current sheet (Zharkova & Khabarova, 2012; Zank et al., 2014;
 37 Khabarova et al., 2015, 2017), and Earth magnetosphere (Øieroset et al., 2002; Angelopoulos et al., 2008;
 38 Chen et al., 2008). The energetic particles generated by magnetic reconnection processes can be detected
 39 via hard X-ray (Holman et al., 2011; Zharkova et al., 2011) and γ -ray (Vilmer et al., 2011) emission in
 40 solar flares, which are often obscured by various transport effects of particles or radiations. More details
 41 can be obtained via in-situ observations of the heliospheric structures by WIND or ACE spacecraft, or the
 42 observations in magnetosphere current sheets (CSs) by Clusters mission (Cattell et al., 2005) or by the
 43 multi-spacecraft Magnetospheric Multiscale Mission (MMS) (Øieroset et al., 2001; Burch et al., 2016),
 44 which can measure particle distributions inside RCSs, while a spacecraft passing through.

45 The recent space observations of current sheets in the magnetosphere and heliosphere (Fujimoto &
 46 Sydora, 2008; Zhou et al., 2009; Huang et al., 2016; Pucci et al., 2017; Eastwood et al., 2018; Phan et al.,
 47 2020) and 2D/3D full kinetic and Hall-MHD simulations (Daughton et al., 2004; Matthaeus & Velli, 2011;
 48 Roytershteyn et al., 2012; Boldyrev et al., 2013; Loureiro & Boldyrev, 2017; Franci et al., 2017; Papini
 49 et al., 2019; Pezzi et al., 2021) had already pointed to a link between reconnection and turbulence. Current
 50 sheets contain a sufficient amount of free energy which is released by instabilities in collisionless plasmas
 51 at the smallest, kinetic scales often revealing in both hybrid-kinetic and Hall-MHD turbulence simulations
 52 the onset of energy transfer at the smallest scales as soon as reconnection is triggered (see for details
 53 Matthaeus & Velli, 2011; Papini et al., 2019; Pezzi et al., 2021, and references therein). The small-scale
 54 turbulence in a vicinity of those CSs was usually associated with spectral breaks in the magnetic fluctuation
 55 spectra near the ion cyclotron frequency Ω_{ci} . At larger scales (low frequencies), there is the characteristic
 56 inertial range of the turbulent cascade, while below ion scales the turbulent spectra shows a clear power
 57 law with spectral indices close to $-2.7 - 2.8$ (Boldyrev et al., 2013; Loureiro & Boldyrev, 2017; Pucci
 58 et al., 2017; Franci et al., 2017; Muñoz & Büchner, 2018). Moreover, the power-laws and spectral breaks
 59 near CSs are very similar to those measured in homogeneous turbulent solar wind plasmas (Chen et al.,
 60 2008; Zhou et al., 2009; Huang et al., 2016; Eastwood et al., 2018; Phan et al., 2020).

61 Also one of the longest-known instabilities connected with reconnection is the lower hybrid drift instability
 62 (LHDI) long suspected to play a role in reconnection (process as observed in space (Cattell et al., 2005;
 63 Chen et al., 2008; Divin et al., 2015; Artemyev et al., 2016) and in the laboratory (Carter et al., 2002). Such
 64 the LHDI occurs near the lower hybrid frequency $\omega_{lh} = \frac{\omega_{pi}}{\sqrt{1 + \omega_{pe}^2 / \Omega_{ce}^2}}$, where $\omega_{pe}(\omega_{pi})$ is the electron (ion)
 65 plasma frequency, Ω_{ce} is the electron cyclotron frequency (Muñoz & Büchner, 2018). Although, all these
 66 observations do not yet have the certain answers as to which processes of a reconnection contribute to the
 67 measured turbulent spectra.

68 The kinetic turbulence in reconnecting current sheets has been extensively investigated (see, for example,
 69 Drake et al., 2003; Fujimoto & Machida, 2006; Fujimoto, 2014; Muñoz & Büchner, 2018; Lapenta et al.,
 70 2020, and references therein). Cattell et al. (2005) observed the electron holes in the separatrix regions
 71 similar to the prediction of 3D PIC simulations (Drake et al., 2003) that are considered to be the nonlinear
 72 evolution of the bump-in-tail instability, or Buneman instability (Omura et al., 1996). Lapenta et al. (2020)
 73 identified the two regimes of turbulent fluctuations in current sheets: one in the outflow leading to a turbulent

74 regime where the fluctuations involve both fields and particles and the other in the inflow and separatrix
75 region, which involves only the electromagnetic fields, without significantly affecting the particles. The
76 two regimes differ much in practical consequences. The outflow regime is capable of inducing a strong and
77 turbulent energy exchange as well as strong anomalous momentum exchange dominated primarily by the
78 electrostatic term in Ohm's law. The inflow regime, in contrast, does not lead to substantial fluctuations in
79 the field-particle energy exchange nor significant anomalous viscosity or resistivity limiting turbulence
80 to the electromagnetic fields only. However, the authors presented a more intuitive interpretation of the
81 detected turbulence obtained from PIC simulations without linking it to the regimes of particle acceleration
82 during magnetic reconnection in a presence of magnetic islands.

83 In order to understand these kinetic instabilities generated in reconnecting current sheets one needs to
84 explore acceleration of particles dragged into the reconnection region and to investigate the turbulence
85 generated by them. For this reason, we need to refresh our views about the properties of accelerated
86 particles gained during their passage through a reconnecting current sheet with a single and multiple
87 X-nullpoints and to explore which of them, if any, can lead to the formation of turbulence and in what
88 locations. Since the plasma turbulence introduced by beam instabilities is, in general, inherently a 3D
89 problem in PIC simulations (Goldreich & Sridhar, 1995; Siversky & Zharkova, 2009; Muñoz & Büchner,
90 2018), it requires the simulation domain for acceleration of particles in current sheets to be a 3-dimensional
91 one.

92 The theoretical and numerical studies of magnetic reconnection are typically performed using a simplified
93 system of 2D anti-parallel reconnecting magnetic fields with an additional out-of-plane guiding magnetic
94 field (B_g) in the third dimension. Such RCSs with a finite B_g are observed in Earth magnetopause (Silin &
95 Büchner, 2006) and at the impulsive phases of flares and CME eruptions (Fletcher et al., 2011). Owing to
96 large magnetic field gradients and curvatures surrounding the reconnection sites, combined with strong
97 gradients of the plasma temperature and density, the electromagnetic fields vary dramatically inside
98 reconnecting current sheets (RCSs) (Shay et al., 2016; Xia & Zharkova, 2020).

99 Furthermore, thin elongated RCSs formed in the diffusion region between the reversed magnetic field
100 lines are often broken down by tearing instability into multiple islands, or O-type nullpoints separated
101 by X-nullpoints (Furth et al., 1963; Loureiro et al., 2007; Bhattacharjee et al., 2009). The presence of
102 magnetic islands in reconnecting current sheets was demonstrated by magnetohydrodynamic (Biskamp,
103 1986; Loureiro et al., 2005; Drake et al., 2006; Lapenta, 2008; Bárta et al., 2011) and kinetic simulations
104 (Huang & Bhattacharjee, 2010; Karimabadi et al., 2011; Markidis et al., 2012). Such chain of magnetic
105 islands have been identified in many solar flares Lin et al. (2005); Oka et al. (2010); Bárta et al. (2011);
106 Takasao et al. (2012); Nishizuka et al. (2015) and CMEs (Song et al., 2012), in the in-situ observations in
107 the heliosphere (Zharkova & Khabarova, 2012; Khabarova et al., 2015, 2021) and Earth magnetotail (Zong
108 et al., 2004; Chen et al., 2008; Wang et al., 2016).

109 In the case of full 3D RCSs, the guiding field is accepted varying in time and space. In some configurations
110 of 3D RCSs, the out-of-plane variations of the helical magnetic structures become pretty significant, due
111 to the kink instability, obscuring current sheet structures and making it hard to define clear X-nullpoints
112 (Daughton et al., 2011; Egedal et al., 2012). A strong guiding field B_g can suppress the out-of-plane
113 kink instability while leaving the concept of magnetic islands still applicable (Lapenta & Brackbill, 1997;
114 Daughton, 1999; Cerutti et al., 2014; Sironi & Spitkovsky, 2014). Nevertheless, further studies have shown
115 that both cases do not significantly change the scenarios of energy conversion and particle acceleration
116 in 3D RCSs, because the dominant mechanisms of particle energisation remain the same as in the 2.5D
117 scenario (Hesse et al., 2001; Zharkova et al., 2011; Guo et al., 2014; Dahlin et al., 2017).

118 Depending on magnetic field topologies, the presence of a guiding field in an RCS would cause partial or
119 full charge separation between electrons and ions (Zharkova & Gordovskyy, 2004; Pritchett & Coroniti,
120 2004) because they gyrate in the opposite directions in a magnetic field. This, in turn, can lead to the
121 preferential ejection of the oppositely charged particles into the opposite semiplanes of CSs, or opposite
122 footpoints of reconnecting loops. It makes the hard X-ray sources to be spatially separated from the γ -ray
123 sources in the opposite footpoints of reconnecting magnetic loops (Lin et al., 2003; Hurford et al., 2003,
124 2006). This charge-separation phenomenon is also confirmed in the laboratory experiments (Zhong et al.,
125 2016).

126 Furthermore, there is a polarisation electric field in RCSs confirmed by 3D PIC simulations (Fujimoto,
127 2006; Zenitani & Hoshino, 2008; Cerutti et al., 2013; Fujimoto, 2014) but its nature was not clear and
128 sometimes mixed with the parallel electric field of accelerated electrons. Then it was shown that the
129 polarisation electric field is induced across the reconnection current sheet midplane by the separation of
130 particles of opposite charges (electrons and protons) during their acceleration in current sheets with a
131 strong out-of-plane guiding field; and its magnitude is much larger (by two orders of magnitude) than a
132 reconnecting electric field itself (Zharkova & Agapitov, 2009; Siversky & Zharkova, 2009). Furthermore,
133 the spatial profiles of a polarisation electric field were found dependent on magnetic field topologies
134 because this electric field is induced by the separated electrons and protons (Zharkova & Agapitov, 2009;
135 Siversky & Zharkova, 2009; Zharkova & Khabarova, 2012). The presence of polarisation electric field
136 is shown to explain the in-situ observations of ion velocity profiles during spacecraft crossings of the
137 heliospheric current sheet, which are found to follow closely the profiles of polarisation electric field
138 (Zharkova & Khabarova, 2012, 2015). Therefore, the ambient plasma feedback to a presence of accelerated
139 particles during their passage through reconnecting current sheets is very important for the particles of
140 opposite charges.

141 However, the particles of the same charge entering the 3D RCS from the opposite edges would also lead
142 to different energy gains by the particles with the same charge (Siversky & Zharkova, 2009; Zharkova
143 & Khabarova, 2012; Khabarova et al., 2020). The particles that enter the RCS from the side opposite to
144 that, to which they to be ejected, are classified as “transit” particles, while the particles entering the RCS
145 from the same side where they to be ejected to, are classified as “bounced” particles. The transit particles
146 gain significantly more energy because they become accelerated on their way to the midplane where the
147 main acceleration occurs, while bounced particles lose their energy while they approach the midplane,
148 thus, gaining much less energy in the current sheet (Zharkova & Gordovskyy, 2005; Zharkova & Agapitov,
149 2009; Siversky & Zharkova, 2009; Zharkova & Khabarova, 2012).

150 The energy difference between the transit and bounced particles creates the particle beams with ‘bump-
151 in-tail’ velocity (energy) distributions, which could trigger different two beam instabilities (Buneman,
152 1958) and naturally generate plasma turbulence. Although, strong turbulence very often appears in the
153 off-plane direction at the very early stages of 3D PIC simulations of magnetic reconnection (Daughton
154 et al., 2011; Egedal et al., 2012) that obscures any other types of turbulence present in the simulations at
155 later times. And, of course, the kinetic turbulence generated in current sheets can also contribute to particle
156 acceleration by modifying the parameters of accelerated particles (Zharkova & Agapitov, 2009; Drake
157 et al., 2010; Matthaeus & Velli, 2011; Fujimoto, 2014; Muñoz & Büchner, 2016; Huang et al., 2017; Trotta
158 et al., 2020).

159 The goal of the current research is to explore kinetic turbulence generated by accelerated particles in
160 reconnecting current sheets with multiple X- an O-nullpoints based on the specifics of particle acceleration
161 on 3D magnetic field topologies. As one can note, the accelerated particles definitely gain non-Maxwellian

162 (power-law) distributions during their acceleration in current sheets. Hence, we will attempt to explore
 163 the conditions in the phase and frequency domains for energetic particle beams to maintain the pressure
 164 anisotropy (Le et al., 2013) and their effects on instabilities generated due to asymmetric acceleration by a
 165 reconnection electric field. In addition, we wish to explore anisotropy of the electric and magnetic field
 166 fluctuations in turbulence along and perpendicular to the local mean magnetic field \mathbf{B}_{m0} (Howes et al.,
 167 2008; Boldyrev et al., 2013) for different locations inside a reconnection region.

168 The simulation model and magnetic field topology are described in section 2, the results of simulations
 169 of energetic particles and generate turbulence for a current sheet with single and multiple X-nullpoints are
 170 presented in section 3 and the general discussion and conclusions are drawn in section 4.

2 SIMULATION MODEL

171 2.1 Magnetic field topology

172 In the current paper, unlike our previous simulation (Siversky & Zharkova, 2009; Xia & Zharkova, 2020),
 173 we do not separate the original and induced electromagnetic fields, and adopt the self-consistent 3D PIC
 174 simulation to investigate particle acceleration in magnetic islands generated by a magnetic reconnection.
 175 Although, we will use the previous results (Xia & Zharkova, 2020) about particle acceleration in the similar
 176 reconnection scenarios to evaluate possible mechanisms of the recorded kinetic turbulence. We extend the
 177 3D simulation region to a larger domain compared to the previous 2.5D studies (Siversky & Zharkova,
 178 2009; Muñoz & Büchner, 2016).

179 The simulations start with a Harris-type current sheet in the $x - z$ plane:

$$\begin{aligned} \mathbf{B}_x &= -\frac{2L_x}{L_z} \delta B_0 \sin\left(2\pi \frac{z - 0.5L_z}{L_z}\right) \cos\left(\pi \frac{x}{L_x}\right), \\ \mathbf{B}_y &= B_{0y}, \\ \mathbf{B}_z &= B_{0z} \tanh\left(\frac{x}{d_{cs}}\right) + \delta B_0 \cos\left(2\pi \frac{z - 0.5L_z}{L_z}\right) \sin\left(\pi \frac{x}{L_x}\right), \end{aligned} \quad (1)$$

180 where d_{cs} is the half thickness of RCS. The B_0 is the initial guiding field, which is perpendicular to the
 181 reconnection plane. In the presented simulation $b_g = B_{0y}/B_{0z} = 1.0$. The initial density variation across
 182 the CS is:

$$n = n_b + n_0 \operatorname{sech}^2\left(\frac{x}{d_{cs}}\right), \quad (2)$$

183 where n_0 is the ambient density in a current sheet, n_b is the density of an accelerated particle beam and d_{cs}
 184 - a current sheet thickness.

185 2.2 Particle Motion Equations

186 The motion of a charged particle in an electromagnetic field \vec{E} and \vec{B} is computed by the relativistic
 187 Lorentz equations:

$$\frac{d\vec{p}}{dt} = q(\mathbf{E} + \mathbf{V} \times \mathbf{B}), \quad (3)$$

$$\frac{d\vec{r}}{dt} = \frac{\vec{p}}{m\gamma}, \quad (4)$$

188 where $\mathbf{V}(= \vec{p}/m\gamma)$ and \vec{r} are the particle velocity and position vectors, q and m are the charge and the
 189 rest mass of the particle. \vec{p} is the momentum vector and γ is the corresponding Lorentz factor defined as
 190 $\gamma = 1/\sqrt{1 - V^2/c^2}$. \mathbf{E} and \mathbf{B} are calculated from the initial electro-magnetic fields and the ones induced
 191 by accelerated particles as described in section below.

192 2.3 The plasma feedback

193 Similarly to the early paper (Xia & Zharkova, 2020), in the initial PIC approach we split the
 194 electromagnetic field \mathbf{E} and \mathbf{B} into two components, the background \mathbf{E}_{static} and \mathbf{B}_{static} , and the local
 195 self-consistent $\tilde{\mathbf{E}}$ and $\tilde{\mathbf{B}}$ induced by the particle motions (Eq. 4): $\mathbf{B} = \tilde{\mathbf{B}}_{static} + \tilde{\mathbf{B}}$, and $\mathbf{E} = \tilde{\mathbf{E}}_{static} + \tilde{\mathbf{E}}$.
 196 Then the fluctuation fields are calculated by the Maxwell solver:

$$\frac{\partial \tilde{\mathbf{E}}}{\partial t} = c^2 \nabla \times \tilde{\mathbf{B}} - \frac{1}{\epsilon_0} (\mathbf{j}_e + \mathbf{j}_p), \quad (5)$$

$$\frac{\partial \tilde{\mathbf{B}}}{\partial t} = -\nabla \times \tilde{\mathbf{E}}, \quad (6)$$

197 where \mathbf{j}_e and \mathbf{j}_p are the current densities of electrons and protons updated by the particle solver. The
 198 Maxwell's equations are solved by standard finite-difference time-domain method (FDTD) numerically.
 199 This approach can help us to identify the effect of the ambient particles that are drift into a current sheet
 200 and accelerated. Then we rerun the 3D PIC simulations by relaxing all electromagnetic fields and following
 201 the reconnection process until the certain time when maximal turbulence is formed

202 2.4 Numeric method

203 After clarifying the accelerated particle dynamics by splitting the electro-magnetic fields as above, we
 204 rerun the PIC simulations with VPIC code by relaxing electromagnetic fields of particles and allowing
 205 them to interact together with the initial electromagnetic field to reflect a reconnection process initiated by
 206 some perturbation. PIC simulations were carried out using fully relativistic 3D VPIC code (Bowers et al.,
 207 2008). Our setup is somehow similar to the one employed in Muñoz & Büchner (2018) with some essential
 208 differences. The RCS thickness was $d_{cs} = 0.5d_i$ (versus $0.25 d_i$ by Muñoz & Büchner, 2018), where d_i is
 209 the ion inertial length. We chose a mass ratio $m_i/m_e = 100$, a temperature ratio $T_i/T_e = 5$, a background
 210 plasma density $n_b/n_0 = 0.2$ versus $n_b/n_0 = 1.0$ accepted by Muñoz & Büchner (2018), and a frequency
 211 ratio $\omega_{pe}/\Omega_{ce} = 1.5$, where ω_{pe} is the electron plasma frequency and Ω_{ce} is the electron gyro-frequency.
 212 Plasma beta is estimated as $\beta_e = \beta_i = 2\mu_0 n_0 k_B T_i / B_0^2 \approx 0.012$ versus 0.016 in Muñoz & Büchner (2018).

213 Following the approach discussed by Siversky & Zharkova (2009), for the current sheet thickness equal
 214 to the ion inertial length, d_i , we select the number of cells across the current sheet in a PIC simulation have
 215 to be $\frac{d_i}{\lambda_D} = cm_i / (kT)$, which is $3 \cdot 10^3$ for the solar corona temperature or $3 \cdot 10^4$ for the magnetosphere. In
 216 order to reduce this number, Drake et al. (2006) used a reduced magnitude for the speed of light $c = 20V_A$
 217 $= 6 \cdot 10^6 \text{ m s}^{-1}$, where V_A is the Alfvén velocity. Another way to reduce the number of cells was used in
 218 the PIC simulation carried out by Karlický (2008), who considered the high-temperature electron–positron
 219 plasma, for which the ratio d_i/λ_D was as low as 10.

220 The simulation box size is $L_x \times L_y \times L_z = 12.8d_i \times 1.6d_i \times 51.2d_i$ with grid number $512 \times 64 \times 2048$
 221 using 100 particles per cell. In order to avoid the problem with the small Debye length λ_D , only a small
 222 fraction of the plasma particles (with density of $10^{12} \text{ m}^{-3} = 10^6 \text{ cm}^{-3}$) is included in the current PIC
 223 simulation. This makes the ratio $\frac{\lambda_D}{d_i}$ in the current simulations is the order of 0.0192, e.g. the mesh step
 224 ratio $d/\lambda_D=1.3$ that is close to that of 1.4 used by Daughton et al. (2011) for the same VPIC code. Hence,

225 this mesh is safe and does not require any corrections on possible numerical stabilities of the explicit PIC
226 code using the linear shape function (Birdsall & Langdon, 1991).

227 Along the direction x , the conducting boundary condition for the electromagnetic field and open boundary
228 condition for particles are used. The periodic boundary conditions are applied along z - and y -directions
229 (in the current sheet midplane $X=0$) to the electromagnetic field and particles. We use a real speed of light
230 without scaling it to Alfvén speed, while using a reduced mass ratio between protons and electrons, like
231 Siversky & Zharkova (2009) did. This approach is valid for the coronal magnetic fields only while the
232 density would need to be modified if applied to current sheets in the magnetosphere or heliosphere as the
233 applied setting can lead to larger than real Alfvén velocities in the Earth magnetosphere.

234 To trigger a magnetic reconnection in the plane with magnetic islands, we introduce a small perturbation
235 at the beginning of the simulation, which is written in terms of $(\delta B_0 \dots)$ in Eq. (1), where $\delta B_0 = 0.03 B_{0z}$. It
236 comes from an out-of-plane vector potential, $\delta \mathbf{B}_0 = \nabla \times \delta A_y$, where $\delta A_y \propto \cos\left(2\pi \frac{z-0.5L_z}{L_z}\right) \cos\left(\pi \frac{x}{L_x}\right)$
237 satisfying $\nabla \cdot \mathbf{A} = 0$. This spatial distribution helps us to set the fast reconnection to occur near the centre
238 of the simulation box in Figure. 4(a-d), similar to that reported earlier (Daughton et al., 2011).

239 We will gather the kinetic turbulence in the whole simulation region at the particular moment when
240 turbulence is stabilised (experiment 1). Also we will collect the kinetic turbulence data by a hypothetical
241 spacecraft sampling the simulation domains at a few particular points with respect to the local mean
242 magnetic field \mathbf{B}_{m0} (experiment 2). Because the streaming instabilities are often observed in the separatrices
243 (current sheet midplanes) and at the exhaust regions (Cattell et al., 2005; Lapenta et al., 2011; Markidis
244 et al., 2012; Zhang et al., 2019; Lapenta et al., 2020), the positions of the virtual spacecraft are to be
245 simultaneously located in the three points close to the separatrices at different distances away from the
246 X-nullpoints inside the current sheet structure that forms a magnetic island.

247 Given the relativistic velocities of accelerated particles, which generate the turbulence within a very short
248 timescale after the acceleration start, we can safely assume that any Doppler shifts in the frequencies of
249 turbulence induced by accelerated particles caused by the motion of the ambient plasma particles inside a
250 current sheet are negligible, because the motion of charged particles in an RCS strictly follows rigidly the
251 magnetic field topology completely forgetting its initial velocity at the entry (Zharkova & Gordovskyy,
252 2004, 2005; Dalla & Browning, 2005; Wood & Neukirch, 2005; Siversky & Zharkova, 2009; Xia &
253 Zharkova, 2018, 2020).

3 SIMULATION RESULTS

254 3.1 Single X-nullpoints

255 In order to understand the physical nature of the turbulence generated inside RCSs with magnetic islands,
256 let us use the models described in our previous papers (Xia & Zharkova, 2018, 2020), which compared
257 particle acceleration in a single X-nullpoint and in coalescent and squashed magnetic islands. The current
258 sheet with a single X-nullpoint was described by the set of equations with the following magnetic field
259 components: $B_z = -B_0 \tanh\left(\frac{x}{d}\right)$, $B_x = -B_0 \xi_x\left(\frac{z}{a}\right)$; $B_y = -B_0 \xi_y$, and a reconnection electric field $E_y =$
260 250 V/m with the current sheet plane to be $x - z$ plane, where d is a current sheet thickness and a is its
261 length (Xia & Zharkova, 2018).

262 In the PIC approach, there is also a feedback of the ambient plasma considered to the presence of
263 accelerated particles by calculating the electric and magnetic fields induced by accelerated particles as
264 described by Eq.(3) and (4) in section 2.1.2 of Xia & Zharkova (2020). Similarly to Siversky & Zharkova

265 (2009), in the PIC code the authors (Xia & Zharkova, 2020) introduced the initial (static) background
 266 electric and magnetic fields (Verboncoeur et al., 1995; Bowers et al., 2008) and then followed particle
 267 acceleration as well as their induced electric and magnetic fields in the current sheets with the single or
 268 multiple X-nullpoints (with magnetic islands).

269 This approach can help us to separate the original magnetic field configuration of the magnetic
 270 reconnection from that induced by the plasma feedback due to a presence of accelerated particles.
 271 This separation helps to discover potential triggers of plasma turbulence inside these complex magnetic
 272 configurations.

273 3.1.1 Polarisation electric field

274 The trajectories of electron and protons calculated in the RCS near a single X-nullpoint for a strong
 275 guiding field B_y reveal a significant difference between the acceleration paths of the particles with opposite
 276 charges. The particles with different charges are shown separated into the opposite sides from the RCS
 277 midplane and then ejected to the opposite semi-planes (Siversky & Zharkova, 2009; Xia & Zharkova, 2018,
 278 2020). For a given magnetic topology, energetic electrons can primarily be ejected to the $x > 0$ semi-plane,
 279 while protons to the $x < 0$ semi-plane.

280 One important outcome of this separation is the polarisation electric fields induced by the separated
 281 particles with opposite charges across the current sheets. This polarisation electric field δE_x shown in
 282 Fig. 1 is perpendicular to the RCS midplane, and it is much larger than the reconnecting electric field
 283 E_{y0} induced by the magnetic reconnection process. A polarisation electric field was first reported in the
 284 2D PIC simulations by Arzner & Scholer (2001); Fujimoto (2006) and was assigned to particle's inertia
 285 motion. However, the particles passing through 2D current sheets do not gain much energy (Litvinenko &
 286 Somov, 1993; Litvinenko, 1996) and, as result, the polarisation electric field induced by these accelerated
 287 particles owing to separation by inertia would have low magnitudes, in comparison with the reconnection
 288 electric field magnitude accelerating particles. Only later by considering acceleration of particles in 3D
 289 current sheets with a strong guiding field (Zharkova & Gordovskyy, 2004; Pritchett & Coroniti, 2004;
 290 Zharkova & Gordovskyy, 2005; Pritchett, 2005), this polarisation electric field was shown to be enforced
 291 by significant energy gains by all particles and the separation of electrons from protons/ions across the
 292 current sheet midplane. This separation of very energetic electrons and protons generates a significant
 293 polarisation electric field exceeding by up to two orders the reconnection electric field magnitude (Zharkova
 294 & Agapitov, 2009; Siversky & Zharkova, 2009; Zharkova & Khabarova, 2012).

295 In our further simulations, the plasma density is accepted to vary as $10^8 m^{-3}$ and $10^{12} m^{-3}$. The
 296 polarisation electric field distributions are found sensitive to the ambient plasma density as shown in Fig.2
 297 (b). if the density is low, the particle separation is more distinguishable in the phase space as shown in
 298 Fig.2(a, c). However, the polarisation electric field induced in the more rarified ambient plasma is lower
 299 than in the dense plasma. This happens, we believe, because the gradient of magnetic field (the first term in
 300 Eq.5) remains the same while being much smaller than the currents of accelerated electrons and protons,
 301 which are increased for more dense plasma, thus, making higher the resulting electric field E_x induced by
 302 these accelerated particles in denser plasma.

303 Besides, there is a bump-in-tail at high energy electrons in the spectrum of Fig.2(d) which is clearly seen
 304 for lower density plasma. When the polarisation electric field, E_x , becomes larger with a larger density
 305 (the charged particle density should also increase) as shown in Fig.2(b), the preferential ejection becomes
 306 less clear, and the bump-in tail in the particle energy spectrum is smoothed out. Although, this does not

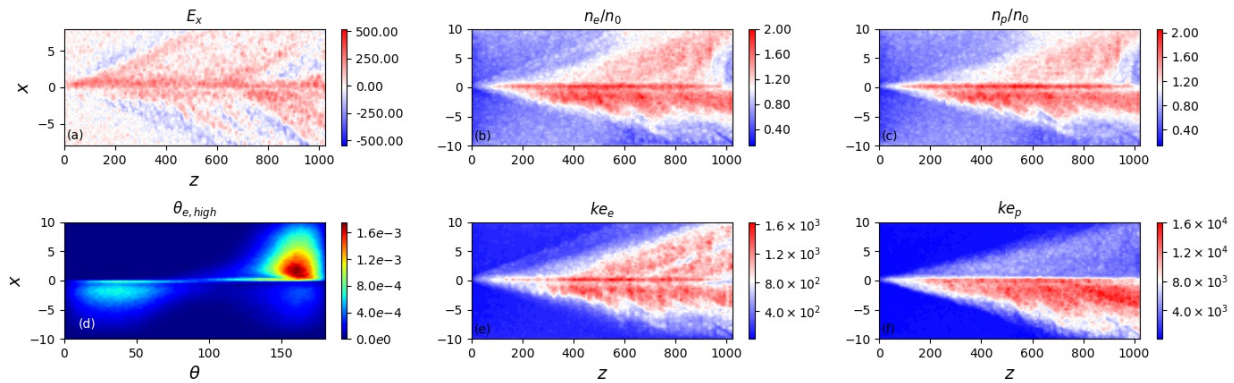


Figure 1. The 3D simulations at $t = 8 \times 10^{-3}$ s: (a) the polarisation electric field E_x (V/m) across the current sheet midplane; the densities of electrons (b) and (c) protons in $x - z$ plane normalised to the initial density (n_0); (d) the pitch-angle distribution of accelerated electrons about the midplane with the colour bar showing particle density in units of n_0 ; (e) the energy (eV, shown by colour bar) of the accelerated electrons (e) and protons (f). The distances X (from the midplane) and Z (from X-nullpoint) are measured in the units of a ion inertial depth d_i . The magnetic field $B_0 = 10^{-3}$ T, $B_y/B_0 = 0.1$, $B_x/B_0 = 0.02$, and the reconnection electric field $E_0 = 250$ V/m.

307 change the maximum energy gains by particles as shown by the spectra in Fig.2(d), which still remain of
 308 the same order of magnitude for all the simulations with different plasma density.

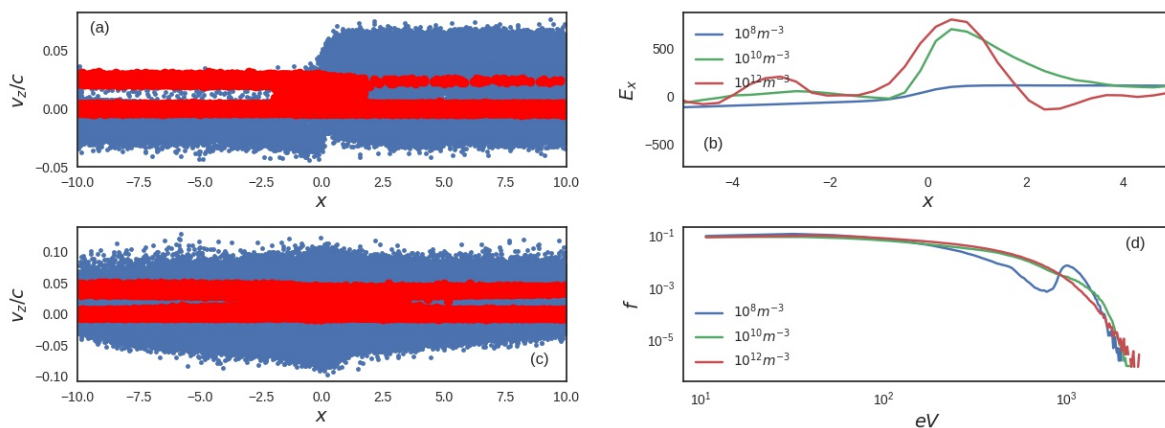


Figure 2. The V_z distributions in the phase space for electrons (blue dots) and protons (red dots) versus a distance X from the midplane (in the units of the ion inertial depth d_i) for the current sheets with the same magnetic field topology as in Fig. 1 (a) $n_0 = 10^8 \text{ m}^{-3}$ and (c) $n_0 = 10^{12} \text{ m}^{-3}$. The polarisation electric fields (in V/m) and the energy spectra for different ambient density are compared in (b) and (d), respectively.

308

309 3.1.2 Plasma turbulence generated by two beams

310 Because of the bump-on tail distribution of the energy spectra of accelerated particles shown of Fig.2(a,c),
 311 there is turbulence formed by Buneman instability (Buneman, 1958), or the electron two stream instability,
 312 which, in addition to the background electro-magnetic fields, leads to fluctuations of electric δE_x , δE_y ,
 313 δE_z and magnetic field vectors $|\delta B_x/B_{x,0}|$, $|\delta B_y/B_{y,0}|$, $|\delta B_z/B_{z,0}| < 1.0 \times 10^{-4}$ in the diffusion region.

314 The fluctuations of magnetic field are rather small as shown in Fig.3, while, the electric field shows very
 315 strong fluctuations (see the left column in Fig. 3). Moreover, the fluctuations of δE_x are found to be larger
 316 than δE_y , δE_z by an order of the magnitude. The small fluctuations of magnetic field can be understood in
 317 terms of the gradient of E_x to occur along x -axis, which shows from Faraday's law, $\partial \mathbf{B} / \partial t = -\nabla \times \mathbf{E}$
 318 that E_x would not change the magnetic field, as demonstrated by $\delta \mathbf{B}$ pictures in Fig.3.

319 As shown in Fig. 3, the electric field fluctuations propagate along z - and y -directions rather than along
 320 the x -direction following the trajectories of accelerated particles. The E_z component represents Langmuir
 321 waves oscillating at $\omega^{-1} \approx 1.3 \times 10^{-7}$ s, which is close to the electron plasma frequency ω_{pe} for the
 322 plasma density of 10^{12} m^{-3} accepted in this simulation (Siversky & Zharkova, 2009).

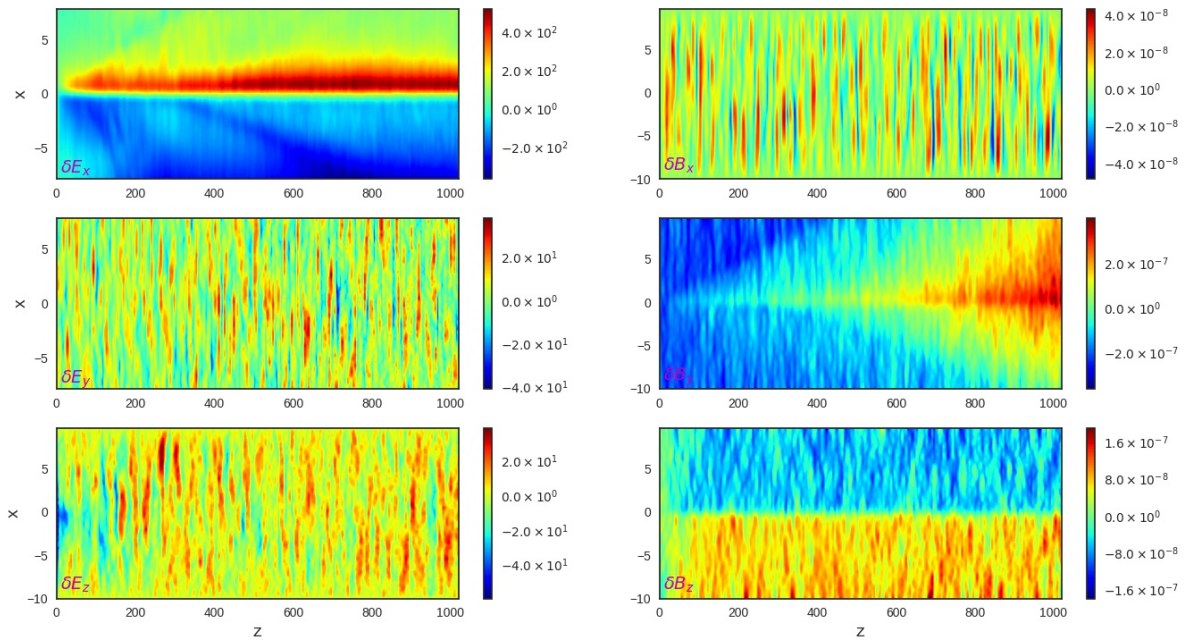


Figure 3. The changes of three components (x,y,z) of the electric vector $\delta \mathbf{E}$ (in V/m , shown by colour bars) (left column) and magnetic $\delta \mathbf{B}$ vector (in T , shown by colour bars) (right column) in a reconnecting current sheet simulated at $t = 5 \times 10^{-4}$ s ($70\Omega_{ci}^{-1}$) for $m_i/m_e = 100$. The magnetic field topology and reconnection electric field are the same as in Fig. 1. The distances X from the midplane and Z (from X -nullpoint) are measured in the units of d_i .

323 3.2 Turbulence in vicinity of multiple X-nullpoints

324 3.2.1 Reconnection with multiple magnetic islands

325 As result of the simulation setting described in section 2, we present simulations for 4 different times
 326 up to $32\Omega_{ci}^{-1}$ when the reconnection reaches the maximum rate similar to Muñoz & Büchner (2018) and
 327 the turbulence is stabilised, as shown in Fig. 4, that achieved later in time because our current sheet is
 328 twice thicker ($d_s = 0.5d_i$). There are multiple small magnetic islands formed at the start, which are later
 329 merged into the large island in the left across the periodic boundary and two smaller islands on the right
 330 hand side as shown in the density and energy distributions of electrons in Fig. 4(c - h). The width of this
 331 crossing-boundary island is increased with the simulation time.

332 Due to the periodic boundary conditions at both ends of the z -axis, the simulation domain represents the
 333 RCSs with a chain of magnetic islands, rather than a single X-nullpoint geometry with open exhausts. The
 334 energy distributions of electrons at $t = 24, 32\Omega_{ci}^{-1}$ (Ω_{ci} is the ion gyrofrequency) show clear asymmetry
 335 of particle distributions with respect to the midplane, due to the presence of a strong guiding field. The
 336 accelerated particle beams of the same charge gain the two-peak energy distributions which naturally
 337 trigger two-stream instabilities leading to the formation of either Langmuir or Bernstein waves depending
 338 on the locations where these kinetic instabilities are generated (Siversky & Zharkova, 2009; Muñoz &
 339 Büchner, 2016, 2018).

340 It has to be noted that our model thickness of the 3D current sheet is twice the thickness used by Muñoz
 341 & Büchner (2018) but it has a much smaller beam density n_b , or the plasma β , inside the diffusion region.
 342 This explains the occurrence of kinetic turbulence in our simulations while it does not appear for the current
 343 sheet with the thickness used for the simulations by Muñoz & Büchner (2018).

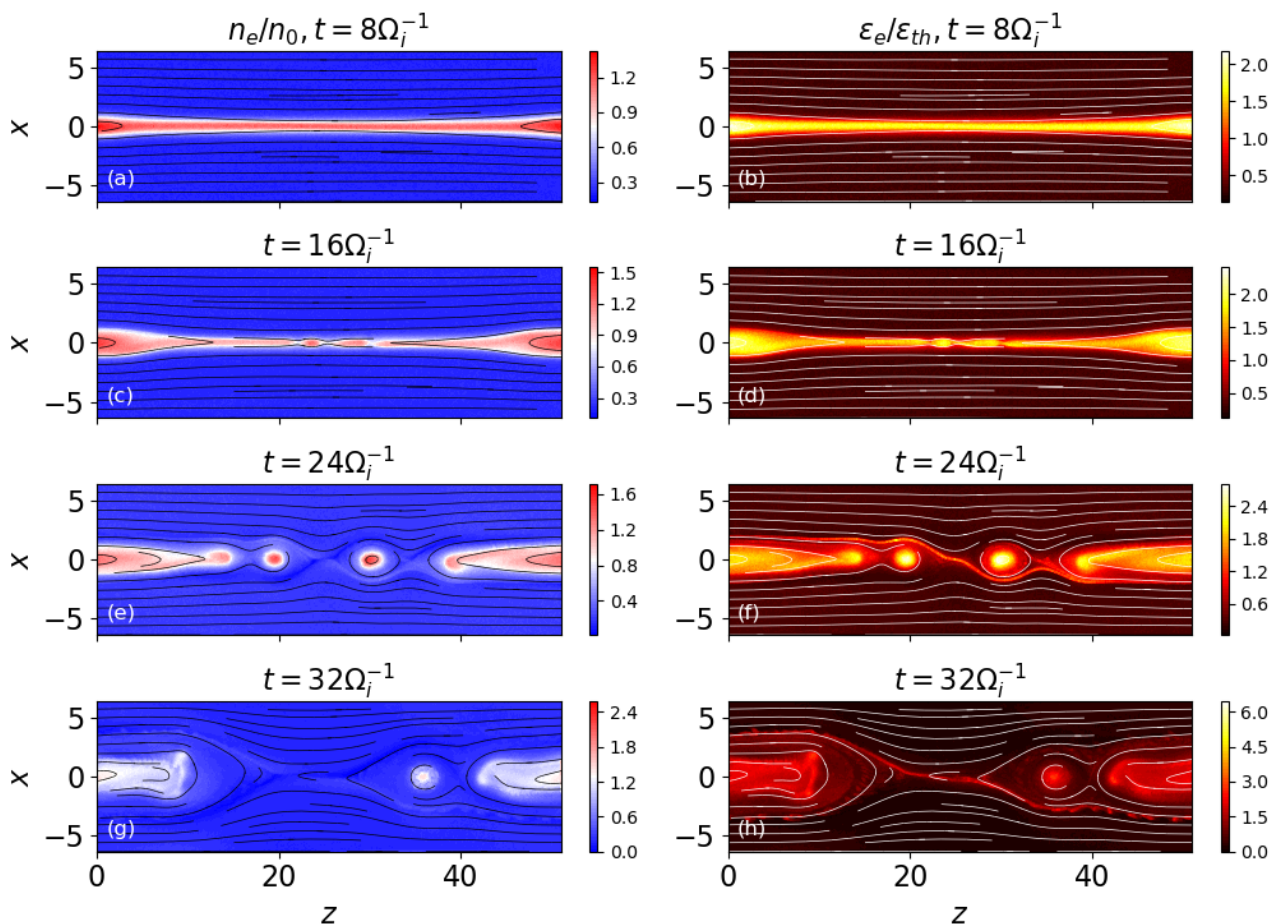


Figure 4. Density (left column) and energy (right column) distributions of electrons on the $x - z$ plane at $y = 0$ at different time: (a, b) $t = 8\Omega_{ci}^{-1}$, (c, d) $t = 16\Omega_{ci}^{-1}$, (e, f) $t = 24\Omega_{ci}^{-1}$, (g, h) $t = 32\Omega_{ci}^{-1}$ for $b_g = 1$.

344 3.2.2 Suppression of kink instability

345 The reconnection process is shown to be weakly affected by the kink instability at a later time, as
 346 evidenced in the isosurface of the electron energy distribution in Figure. 5a. The distributions are similar in
 347 the different $x - z$ planes along the y -direction.

348 If the guiding field is weak and polarisation electric field is weak as well, the reconnecting magnetic fields
 349 would be strongly perturbed by turbulence as reported previously (Daughton et al., 2011; Egedal et al.,
 350 2012). For example, in the $B_g = 0$ case, we observed a twist of the magnetic flux ropes in the simulation
 351 box caused by kink instability after the same running time shown in Figure. 5b. However, with the increase
 352 of the guiding field and the polarisation electric field induced by separated electrons and ions, the twists are
 353 suppressed shown in Figure. 5b.

354 Thus, the locations and the sizes of magnetic islands in different $x - z$ planes would change, which makes
 355 it hard to make statistical analysis depending on the distance from the X-nullpoint on different $x - z$ planes
 356 along the y -direction. Therefore, in order to concentrate on the turbulence other than kink instability, we
 357 should stick to the cases with a strong guiding field ($b_g = 1$), in order to avoid this complication.

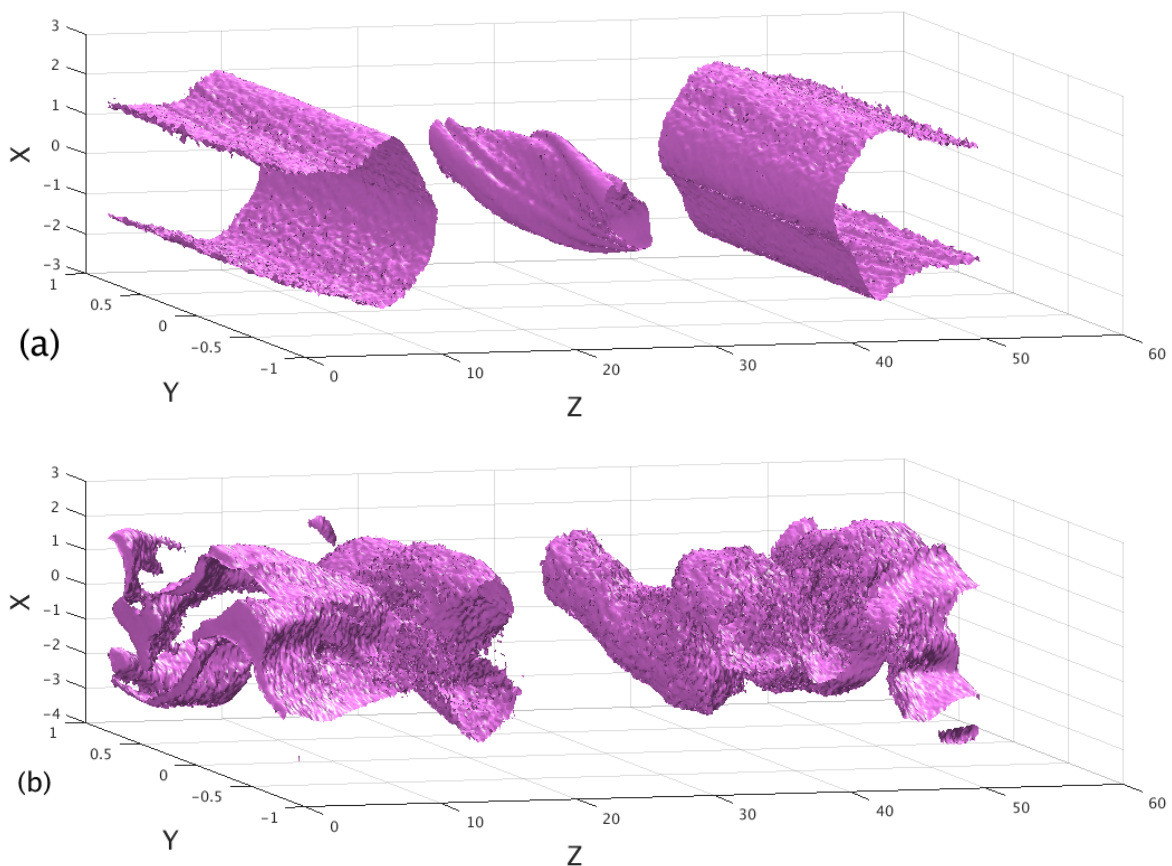


Figure 5. *Upper plot:* Isosurface of the electron energy distribution (the 35% contour of the max energy) for a strong guiding field ($b_g=1$) in the simulation box of Fig. 4 at $t = 28\Omega_{ci}^{-1}$. *Bottom plot:* Isosurface of the electron energy distribution after the same running time from a similar simulation using no guiding field, e.g. $b_g = 0$.

3.2.3 Evaluation of generated turbulence

In our simulation, the ion-scale magnetic islands were formed during magnetic reconnection events as shown in Figure 4(a-h). The size of the largest magnetic island reached $\sim 36d_i$ after $t = 32\Omega_{ci}^{-1}$ in Fig. 4(g, h) when the reconnection reaches the maximum rate and the turbulence is stabilised. Thus, it allows us to study the plasma turbulence developed in the downstream $> 15d_i$ from the X-nullpoint. As described in section 3.2.2, a strong guiding field ($b_g = 1$) is implemented to suppress the out-of-plane kink instability and to keep only the turbulence induced by accelerated particles in the geometry quasi-similar on each $x - z$ plane.

It allows us to get statistical results of turbulence power spectrum collected in the full 3D simulation box including 64 grid points along the y -direction. The isotropised 1D power spectra, similar to the one proposed by Franci et al. (2017), are calculated in the 2D Fourier $x - z$ -plane and averaged/summed over the y -direction. The power spectra of electric (magnetic) fields of the whole box are measured at $t = 32\Omega_{ci}^{-1}$ as $|\mathbf{E}|^2(k)$ ($|\mathbf{B}|^2(k)$) in the Fourier space from the whole 3D simulation region and presented in Fig. 6, where k stands for the wavenumber in the reconnection plane.

In this model, the wave-number spectrum of the magnetic field formed a quasi-stable range from $kd_i = 1$ down to above $kd_e = 1$. A least square fitting of $|\mathbf{B}|^2(k) \propto k^\alpha$ over this range indicates the slope $\alpha \approx -2.7$ suggesting that at this moment there is quasi-stable turbulence built up. Hence, in this large 3D simulation box, the turbulent magnetic field power spectrum in the RCS formed a steady spectral slope $\propto k^{-2.7}$ near the ion inertial length, and a steeper cascade at electron scales at $t = 36\Omega_{ci}^{-1}$. This is consistent with the theoretical predictions and numerical simulations of kinetic turbulence power spectra that predict the index α varying from 2.4 – 3.0 (Boldyrev et al., 2013; Loureiro & Boldyrev, 2017; Pucci et al., 2017; Li et al., 2019).

The power spectrum of the electric field drops significantly at the spatial scale close to the electron inertial scale (the solid line, $k_{de}(n_0)$, and dashed line, $k_{de}(n_b)$, on the right side of the spectra are calculated from the RCS density and background density). This suggests that during the selected time the large-scale turbulent structures are quasi-stable. It looks like the dominant fluctuations in the whole region have rather long periods (or low-frequencies, $\ll \Omega_{ce}$), which are produced by ion beams, while, the spectra show that the electromagnetic energy is strongly damped at the electron characteristic spatial scale (see Fig.6).

Although, in the simulations obtained by Muñoz & Büchner (2018) the 1D turbulence about the X-nullpoint obtained along z direction has spectral indices varying in time, that can be explained by stochastic acceleration of particles near X-nullpoint (Zharkova & Gordovskyy, 2004; Wood & Neukirch, 2005; Dalla & Browning, 2005). We understand this shifting index can be caused by the fact that the 'bump-it-tail' positions in the velocity spectra of accelerated transit particles near X-nullpoint are constantly changing (Xia & Zharkova, 2020) and so does the turbulence, which this beam produces. While at the time of maximum reconnection rate in Muñoz & Büchner (2018) the accelerated particles of the same charge (transit and bounced) gain the maximal energy close to the critical one that causes quasi-stable turbulence with noticeable power-law distribution in the wavenumber domain.

3.2.4 Phase space distributions

Now let us consider the final reconnection configuration with the two large magnetic islands separated by the X-nullpoint and explore with instant virtual spacecrafts the turbulence generated in the three locations A, B, C within the magnetic island (A), close to its edge (B) and close to X-nullpoint (C) in the current sheet $x - z$ plane shown in the upper plot of Fig. 7.

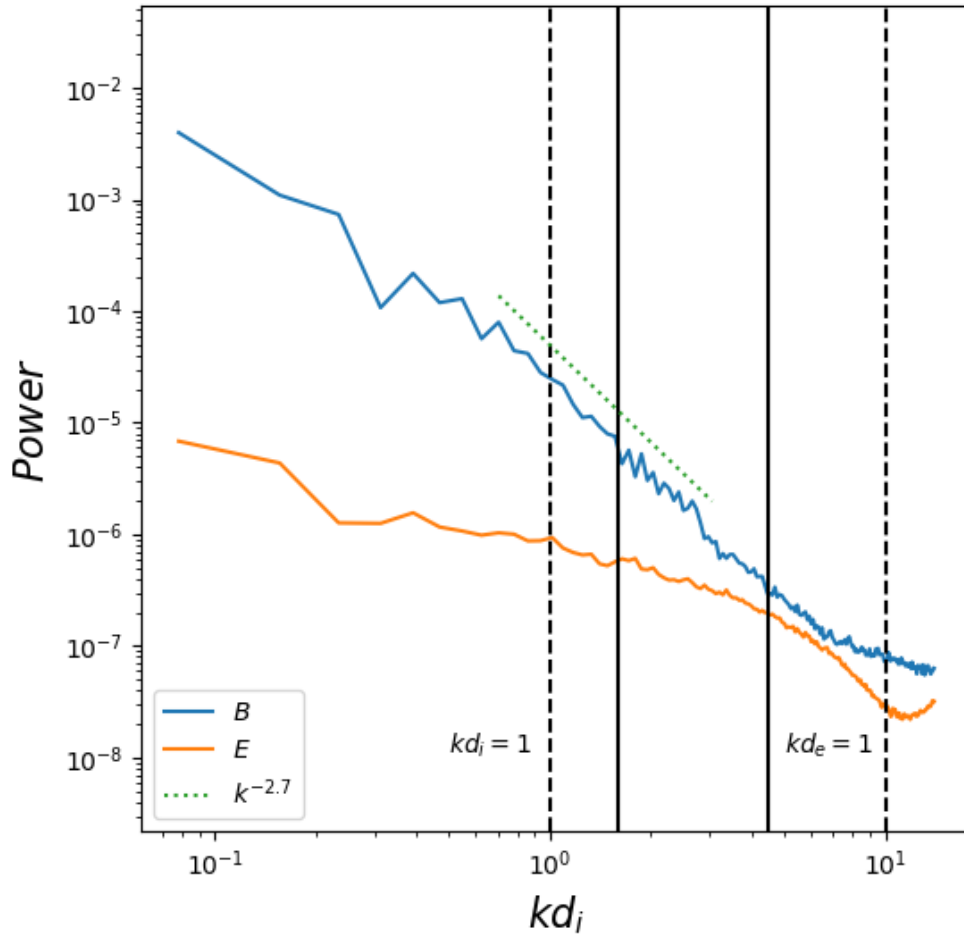


Figure 6. Power spectra of the electric (normalised by $B_0^2 V_A^2$) and magnetic fields (normalised by B_0^2). The wave vector is normalised to d_i^{-1} of n_0 . The corresponding $k_{d_i}(n_0)$, $k_{d_e}(n_0)$ are marked in dash lines. The solid lines indicate the ion gyroscale $k_{\rho_i}^{-1}$ (left) and electron inertial scale calculated by the background density $k_{d_e}(n_b)^{-1}$ (right).

400 In order to establish a link between the turbulence and accelerates particles in the locations of these points,
 401 let us examine the changes of accelerated particle characteristics in the associated plane $x - y$ perpendicular
 402 to the current sheet plane shown by the vertical lines in the upper plot of Fig. 7 in the locations of the
 403 points A and B. This gives a complete 3D presentation of the current sheet, and shows that the accelerated
 404 particles have very specific trajectories in the magnetic topology of a current sheet. In the bottom row of
 405 Fig. 7 we present the particle velocity distributions in $x - y$ plane, e.g. the $x - v_y$ phase space for both ions
 406 (bottom left) and electrons (bottom right) along the direction perpendicular to the reconnection midplane at
 407 the points A and B far away from the X-nullpoint.

408 From the phase space analysis we can speculate that the kinetic turbulence is mainly generated by
 409 accelerated particle beams, which are later found to evolve into a phase-space hole indicating their
 410 breakage: this happens at the distance from the particle entrance in an RCS of about $7d_i$ for electron beams
 411 and at the distances about $12d_i$ for proton beams, where d_i is an ion inertial depth. This was consistent

412 with the previous numerical findings for simulations in different reconnecting regimes (Drake et al., 2003;
413 Muñoz & Büchner, 2016) and the observations in the Earth's magnetotail (Khotyaintsev et al., 2010).

414 The particle distributions demonstrate clear non-Maxwellian features in electron beam distribution
415 showed in the location B in Fig. 7(c): at $z = 15d_i$ (or $\Delta z \sim 7d_i$ away from the main X-nullpoint). There
416 are clearly seen two beams at the distance $x \approx 3.5d_i$: one with lower velocities and another one moving
417 with much higher velocities while revealing a clear fragmented structure. In addition, there are electron
418 holes formed in the phase space between $x = -1.5d_i$ to $1.5d_i$, which can be triggered by the beam-driven
419 lower hybrid instability discussed in the next section 3.3.

420 As the inspecting spacecraft moves deeper into the magnetic island to the location A, there is also the
421 perturbation in the ion phase space found at $z = 10d_i$ (or $\Delta z \sim 12d_i$ away from the X-nullpoint) in Fig.
422 7(b), with the three quasi-parallel arcs located in the region between $x = 0$ to $2d_i$ and a very bright blob of
423 very energetic protons located at $x = 0$ representing the different groups of the ion beams formed during
424 acceleration. At this instance there were no electron beams at the location A, because the electron beams
425 dissipated at the distance $7d_i$ closer to the location B (Fig. 7c), so there should be only the proton ones
426 present at the point A and any turbulence generated in this location has to be produced by proton beams
427 and their interaction with the ambient plasma (Kucharek et al., 2000; Gomberoff et al., 2002).

428 There are no any clear ion holes in the phase space, but these few arcs are found to quickly disappear
429 further in the downstream of the beam that suggest the ion beams become scattered by the plasma turbulence
430 generated by them that is discussed in section 3.3. Therefore, the particle velocity distributions suggest
431 that accelerated electron or ion beams move away from the X-nullpoint until gaining the critical energy
432 to break from this current sheet. The accelerated ions and electrons form different types of two-beam
433 velocity distributions at different regions of the current sheet, thus, producing different types of instabilities
434 (Buneman, 1958; Siversky & Zharkova, 2009; Muñoz & Büchner, 2018; Kucharek et al., 2000; Gomberoff
435 et al., 2002).

436 3.3 Frequency analysis

437 Now let us study the plasma turbulence introduced by the beam instabilities using electric and magnetic
438 fluctuations in the frequency domain.

439 3.3.1 Wavelet analysis

440 After we identified the instability signals in the particle phase space, let us utilise the discrete wavelet
441 transform, which is a powerful tool to analyse time-series data collected by a pinpoint in the domain
442 (Farge, 1992). The signals at different grids along the y -direction were transformed to the wavelet power
443 spectra using Morlet wavelet for the simulation domain and time up to $80 \Omega_{ci}$. The turbulent fields were
444 approximated by a short-time Fourier transform using a sliding Tukey window with an appropriate overlap.
445 Then the results were averaged along the direction of the out-of-plane y -axis and presented at the instances
446 in the positions of virtual spacecrafts located on the grid points along the y -direction at some given (x, z)
447 coordinates (measured in the units of a proton inertial length d_i).

448 Then we record the fluctuations of electric and magnetic fields in the hypothetical locations of probes A,
449 B and C during the acceleration of particles in the RCS. The signals from different probes are separately
450 transformed to the wavelet power spectra using Morlet wavelet. Then the results are averaged over all the
451 probes with the same (x, z) coordinates.

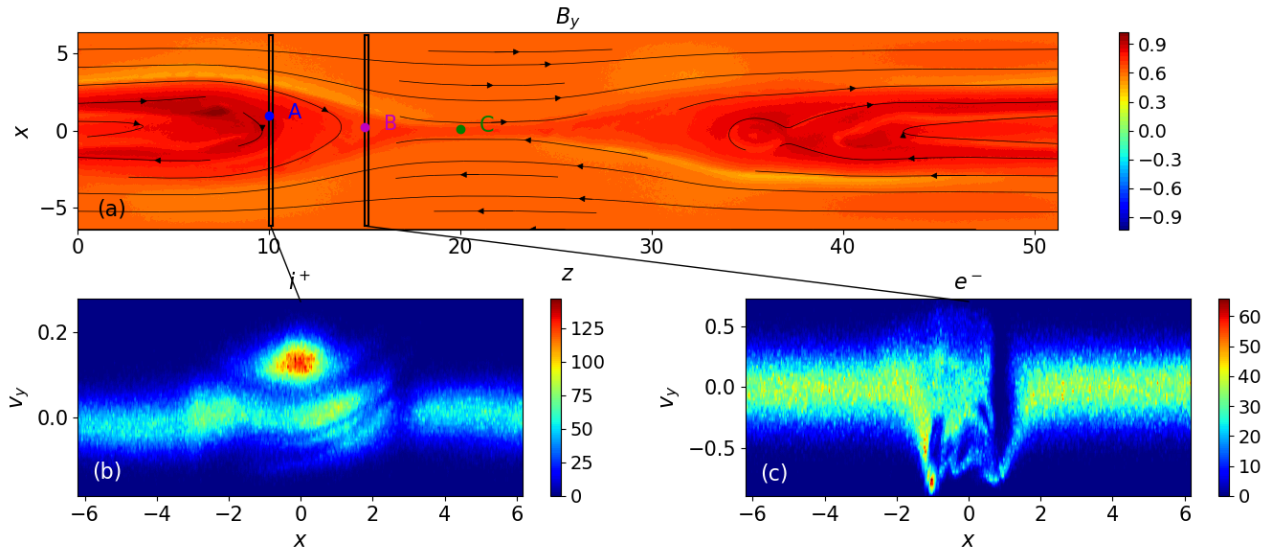


Figure 7. The reconnection plane ($x - z$ magnetic field topology (black solid lines) with the out-of-plane magnetic field component B_y at $y = 0$ coloured (in units of B_z) in panel (a). The simulation started with a strong guiding field ($b_y = 1$). The main X-nullpoint is located at $z = 22, x = 0$. The phase-space distribution functions of velocities (in the units of speed of light c) of accelerated ions (panel b) and electrons (panel c) at difference locations at $t = 36\Omega_i^{-1}$. The phase space structures in (b) and (c) are captured in the vertically elongated boxes with a width of $\Delta y = 0.2d_i$. The distances x and z are measured in the units of d_i . The colour bars in b) and c) define accelerated particle densities in the units of the initial ambient density n_0 . The electromagnetic fields instantly generated at the points A, B, and C are recorded for the further analysis.

452 The wavelet power spectra of both the electric and magnetic field components shared the similar features
 453 at the electron plasma frequency as expected from the results presented in section 3.1.2 and Fig. 3. For
 454 example, Fig. 8 shows the results using the data of the B_x component recorded at point B ($z = 15d_i$,
 455 $x=0.25d_i$), where the electron holes were observed in the phase space in Fig. 7(c) for a period of $5\Omega_{ci}^{-1}$.
 456 Comparing the wavenumber spectra of electromagnetic fields from the whole region (section 3.2), the
 457 wavelet analysis confirmed that the dominant fluctuations have long periods (or low-frequency, $\ll \Omega_{ce}$)
 458 (strips 1 and 2), which can be produced either by fast electron or ion beams. This point we discuss further
 459 in the next section 3.3.2.

460 Furthermore, the wavelet transform revealed wide purple features in the high-frequency region. Fig.
 461 8 depicts several high-frequency signals represented by a wide purple strip 3 below and wide purple
 462 strip 4 above the electron plasma frequency ω_{ce}). Thus, the electromagnetic fields spectra, presented via
 463 the wavenumbers and via the wavelet transform, both indicate the important role of electrons in plasma
 464 turbulence developed in the given location B of the current sheet between its X and O-nullpoints.

465 3.3.2 Frequency spectra of electromagnetic fields

466 We assume that the virtual spacecraft was placed simultaneously at the three different locations: A, B, and
 467 C in Fig 7 with the selected points C \rightarrow A being further away from the X-nullpoint. The selected turbulent
 468 magnetic fields are collected in the surveyed boxes of the size of $\Delta L_x (= 0.2d_i) \times L_y \times \Delta L_z (= 0.2d_i)$
 469 surrounding the selected points in Fig. 7. The values of turbulent fields were averaged in space and time
 470 over $5\Omega_{ci}^{-1}$ using the Fourier transform.

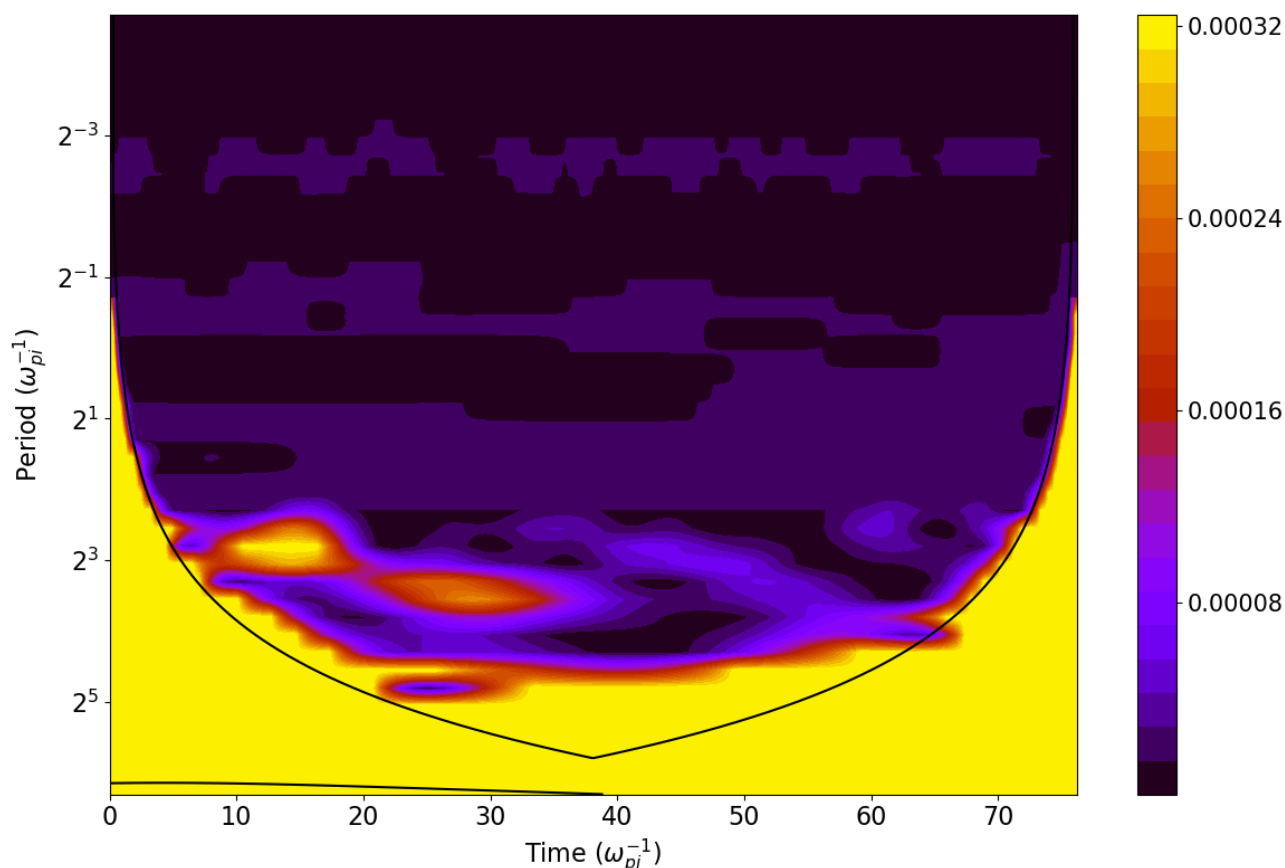


Figure 8. Local wavelet power spectrum of B_x (the purple point B in Figure. 7) at $z = 15$, $x = 0.25$ (in the units of the ion inertial depth d_i) of the time series of B_x components, using Morlet wavelet. Note that X and Z as in other plots are measured. The solid dark curve encloses the regions of $> 95\%$ confidence. By using as a base the X-axis of the frequency spectra shown in Fig. 9, the lower hybrid frequency ω_{lh} can be roughly drawn just above the period of 2^3 (in the units of ω_{pi}^{-1}) where the two strongest lower-hybrid frequency strips 1 and 2 (marked by yellow and red colours) are occurred at the initial times $\leq 36\omega_{pi}$. There are also high frequency strips detected between the electron gyrofrequency Ω_{ce} (between $2^0\omega_{pi}^{-1}$ and $2^1\omega_{pi}^{-1}$) and the electron plasma frequency ω_{pe} (near $2^{-2}\omega_{pi}^{-1}$): the wide purple strip 3 of the high frequency turbulence is located below the period of $2^{-1}\omega_{pi}^{-1}$, while the another purple strip 4 of this high-frequency turbulence is detected above the electron plasma frequency, just below the period mark of $2^{-3}\omega_{pi}^{-1}$.

471 Now let us explore the resulting turbulent components of electro-magnetic fields, \mathbf{B} and \mathbf{E} , in every
 472 grid point of the selected locations (A, B, C) by projecting them onto the background field \mathbf{B}_{m0} . This
 473 will allow us to get the parallel and perpendicular components of the turbulent field and to evaluate more
 474 accurately the turbulence nature in these locations. Note that the distributions presented in Fig. 7 are taken
 475 from the left-hand side of the X-nullpoint. They are the same as those found at the similar distances on the
 476 right-hand side because the model is symmetric with respect to the X-nullpoint. The results are presented in
 477 Fig. 9 for the parallel (left column) and perpendicular (right column) components of the turbulent electric
 478 and magnetic fields.

479 In the sub-high-frequency region, $\Omega_{ce} < \omega < \omega_{pe}$, we found several distinct spikes in all the turbulent
 480 fields at three locations marked by blue, purple and yellow curves. In fact, there are the two small peaks

481 occurring at higher amplitude turbulence at the frequencies below the lower-hybrid frequency, which are
 482 specifically well seen in E_{\perp} , and the another two stronger peaks appearing at lower amplitude turbulence in
 483 parallel and perpendicular electric and magnetic fields at the frequencies between Ω_{ce} and ω_{pe} . Considering
 484 that the periodic boundary condition along z -axis stands for simulating a chain of magnetic islands,
 485 it suggests that the magnetic island pool is fulfilled with these electromagnetic fluctuations above Ω_{ce} .
 486 Furthermore, both high-frequency fluctuations of $\delta\mathbf{E}$ and $\delta\mathbf{B}$ are mainly perpendicular to \mathbf{B}_{m0} . In the
 487 very high-frequency part ($\geq \omega_{pe}$), we first noticed that the perpendicular electric field E_{\perp} at $f > \omega_{pe}$ is
 488 damped significantly as it moves away from the X-nullpoint. In the other words, these high-frequency
 489 waves represented by E_{\perp} are only observable near X-nullpoints (point B and C), which are also clearly
 490 seen in the wide purple patterns (strips 3 and 4) shown in the wavelet plot at these frequencies (see Fig. 8).

491 This high-frequency turbulence is likely to be generated by two-beam instability of electron beams with
 492 'bump-in-tail' distributions in the vicinity of X-nullpoint producing Langmuir waves with the wavelength
 493 of 2 m (or $2d_i$ in the current setting) and a speed of propagation of $(1.7 - 2.0) \cdot 10^7$ m/s (or about $0.07c$)
 494 with the period of $1.5 \cdot 10^{-7}$ s (close to ω_{pe}^{-1}) as reported for current sheet parameters in the solar corona in
 495 section 4.5 of Siversky & Zharkova (2009). Although, as one can observe from Fig. 7c, in some locations
 496 electron beams start moving across the magnetic field lines producing, thus, Bernstein waves that is well
 497 reflected in the peaks of the perpendicular components of the turbulent fields. Both types of these plasma
 498 waves (Langmuir and Bernstein) contribute to the significant peak of high-frequency turbulence seen as in
 499 parallel so in perpendicular components. We believe that significant contribution to the broadband kinetic
 500 turbulence can appear from the electron shear flow instability suggested by Muñoz & Büchner (2018)
 501 which contributes to the perpendicular components of the turbulent electro-magnetic fields.

502 The most puzzling features in the current evaluation are in the low-frequency part: right below Ω_{ce} , we
 503 found a large enhancement in the amplitude of B_{\perp} (and a spike in E_{\parallel}) in the point A. Further down in
 504 the lower frequency region, the amplitudes of B_{\parallel} , B_{\perp} , and E_{\perp} are much larger over a wider range. The
 505 small bump near ω_{lh} (especially in the parallel electric fields near point A at $z = 10, x = 1$, measured in
 506 the units of d_i), where ω_{lh} is the lower hybrid frequency) representing the lower hybrid waves. Since in
 507 this location A we recorded only a very intense proton beams shown in Fig. 7b while electron beams in a
 508 vicinity of point B were broken and formed an electron hole as shown in Fig. 7c, it is safe to assume that at
 509 this instance the turbulence in point A is generated by ion/proton beams (Kucharek et al., 2000; Gomberoff
 510 et al., 2002). There is a noticeable increase of the turbulence close to the lower-hybrid frequency in the
 511 parallel components at the point A and in the perpendicular components in the points A and B (see Fig. 9)
 512 in the parallel B in the left top plot and perpendicular electric field E in the right bottom plot).

513 The lower-frequency turbulence is also seen in the point B shown in the wavelet plot in Fig. 8 as very
 514 bright strips 1 and 2 that could be driven the field-aligned drifts of highly accelerated electrons (Drake
 515 et al., 2003). This turbulence is seen in locations B and C revealing initially a growth of parallel turbulence
 516 and strong levels of oblique lower hybrid (LH) waves at later times (for which we recorded the turbulence).
 517 coinciding with a substantial parallel electron acceleration. In low- β plasmas with intense parallel currents
 518 and both with or without parallel E fields, LH waves are shown to grow even for electron distributions
 519 stable to the parallel Buneman instability, or the electron two-stream instability, and to accelerate electrons
 520 parallel to B very rapidly (McMillan & Cairns, 2006; Fujimoto & Sydora, 2008). This instability may be
 521 seen as the oblique limit of the ion acoustic and Buneman two-stream instabilities at the location where
 522 electrons beam eventually fully dissipates (point B).

523 Moreover, Fujimoto (2014) shown that the intense electron beams can trigger the electron two-stream
 524 instability (ETSI) and the beam-driven whistler instability (WI). The ETSI generates the Langmuir waves,

525 while the WI gives lower hybrid waves. This is, we believe, what is observed in the perpendicular
526 components of turbulence in the locations A and B as shown in Fig. 9, right column, where strong the
527 intense accelerated beams propagate (see Fig. 7b,c).

528 As shown in the b and c plots of Fig. 7, the particle densities in these points A and B have well recorded
529 inhomogeneities of particle densities clearly seen in Fig. 7b,c, which could attribute to the generation of
530 whistler waves in the region near these points as suggested by Zudin et al. (2019). This suggestion is also
531 confirmed by studies of McMillan & Cairns (2007) showing that in plasmas with low beta (as we use in
532 our model) the most unstable mode is not occurring at parallel propagation, but may be at intermediate and
533 very oblique angles. The simulations (McMillan & Cairns, 2007) demonstrate that the very oblique lower
534 hybrid (LH) waves can also arise. The oblique whistler waves are sometimes observed at the lower hybrid
535 frequency in thin current sheets in the heliosphere (Zhou et al., 2009; Artemyev et al., 2016).

536 Also for the point A one can also add generation of the right-polarised resonant instability by very
537 intense proton beams (Kucharek et al., 2000; Gomberoff et al., 2002). In addition, a kinetic branch of
538 Kelvin-Helmholtz instability, can be also enhancing the plasma turbulence near the lower-hybrid frequency
539 since we clearly detected in the locations B and A shown in Fig. 7 the flows of protons travelling from the
540 X-nullpoint to the O-nullpoint.

541 These turbulent electro-magnetic field enhancements near lower-hybrid frequency $f \approx \omega_{lh}$, $f < \Omega_{ce}$,
542 and at higher frequencies $\Omega_{ce} < f < \omega_{pe}$ are also consistent with the dark horizontal stripes in the wavelet
543 power spectrum shown in section 3.3.1. Evidently, by splitting the electromagnetic fluctuations into the
544 parallel and perpendicular direction, we managed to identify the differences between these striped signals
545 in the frequency analysis, which also appeared in the wavelet analysis reported in section 3.3.1. This allows
546 us to assume that the detected turbulence signals could be the real features.

4 DISCUSSION AND CONCLUSIONS

547 In this paper we investigate kinetic turbulence generated by accelerate particles in a reconnecting current
548 sheet (RCS) with X- and O-nullpoints and explore the kinetic turbulence spectra in the wavenumber and
549 frequency domains. We consider reconnection in a thin current sheet with 3D magnetic field topology
550 using 3D particle-in-cell (PIC) approach and carry out the simulations of magnetic reconnection affected
551 by tearing instability. In this simulation we set a larger 3D simulation domain, in which the magnetic
552 reconnection generates two large magnetic islands each $\sim 32d_i$ long. A strong guiding field B_g is
553 implemented to suppress the out-of-plane kink instability and to keep the geometry quasi-similar on each
554 $x - z$ plane. It allows us to get statistical results by averaging the data collected from the 64 grid points
555 along the y -direction.

556 We reiterated our previous findings (Siversky & Zharkova, 2009; Xia & Zharkova, 2020) that during a
557 magnetic reconnection in the presence of a guiding magnetic field, the particles of the same charge drifting
558 into the RCSs from the opposite boundaries would gain different energies, higher for the transit particles
559 and lower for the bounced particles. As result, the high-energy accelerated particles of the same charge
560 form non-Maxwellian distributions with the ‘bump-in-tail’, which leads to Buneman instability (Buneman,
561 1958) or the electron two-stream instability, and generates the observed turbulence (Jaroschek et al., 2004;
562 Siversky & Zharkova, 2009; Drake et al., 2010; Muñoz & Büchner, 2016, 2018). The turbulent magnetic
563 and electric fields generated in the RCS gathered in the large 3D simulation box at the time of $t = 36\Omega_{ci}^{-1}$
564 reveal the turbulent power spectra in the wavenumber space to have a steady spectral slope $\propto k^{-2.7}$ near
565 the ion inertial length, and a steeper cascade at electron scales, which is consistent with the other 3D PIC

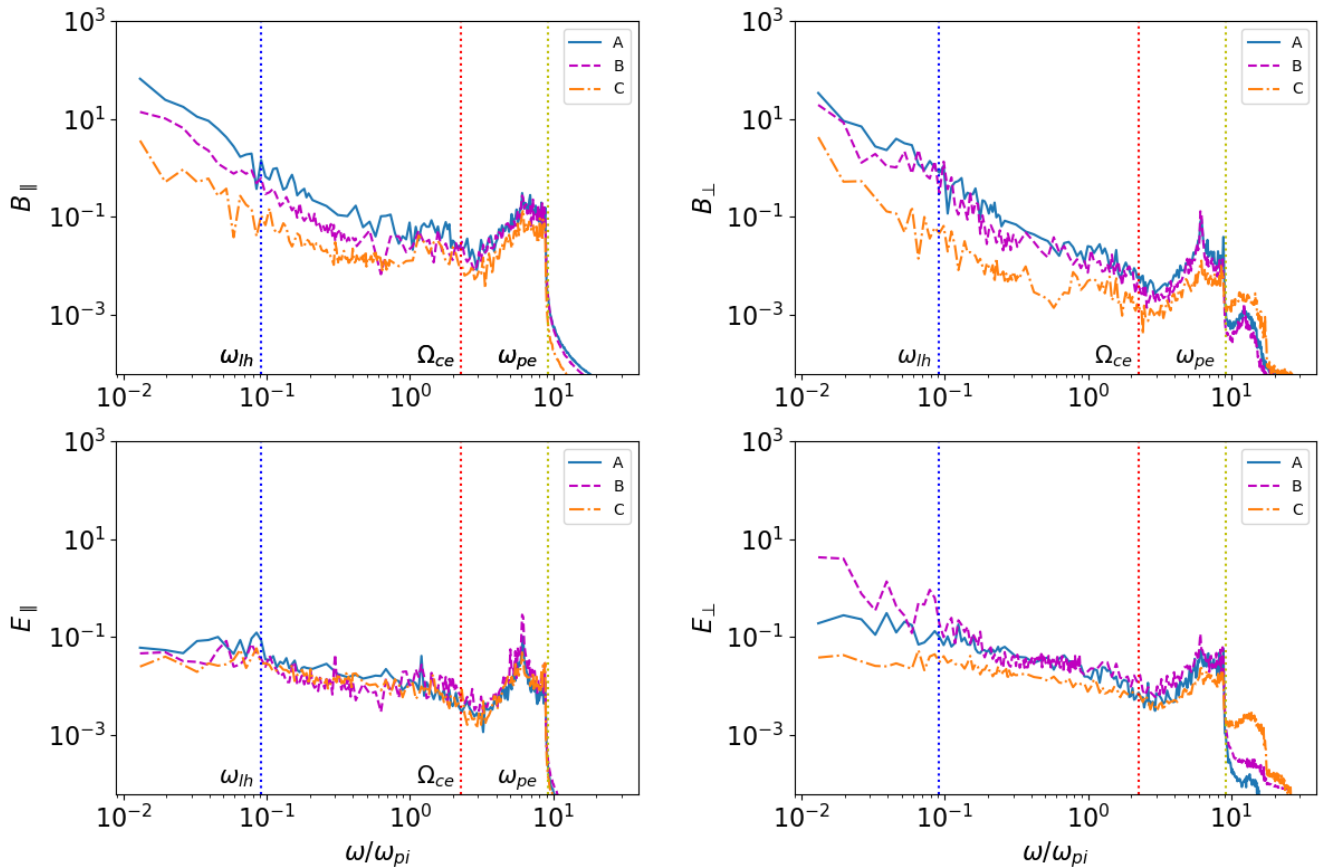


Figure 9. The spectra of different \mathbf{E} and \mathbf{B} components at selected points (marked in corresponding colours in Figure. 7) as functions of the frequency (normalized to ω_{pi}): B_{\parallel} , E_{\parallel} , B_{\perp} , E_{\perp} with respect to the local mean magnetic field in 3D. The characteristic lower-hybrid frequency ω_{lh} , electron gyro frequency Ω_{ce} , and electron plasma frequency ω_{pe} are labelled as vertical dotted lines.

566 simulations of kinetic turbulence (Muñoz & Büchner, 2018; Li et al., 2019) and analytical estimations
 567 (Boldyrev et al., 2013; Loureiro & Boldyrev, 2017).

568 The characteristic waves produced by either electron or proton beams can be identified from the energy
 569 spectra of electromagnetic field fluctuations in the phase and frequency domains and compared with the
 570 particle energy gains. We selected the specific point inside the simulated 3D current sheet close to X and
 571 O-nullpoints to explore the frequencies of generated turbulence in these particular locations. We inspected
 572 the phase space of accelerated particles at this selected time, and identified the two regions with clear
 573 non-Maxwellian distributions: close to the X-nullpoints related to drift instabilities produced by accelerated
 574 electrons and away from X-nullpoints related either to drift instabilities produced by ions.

575 From the phase space analysis we gather the kinetic turbulence and speculate that it can be generated
 576 by accelerated particle beams seen in these locations. These beams are later found to evolve into the
 577 phase-space hole indicating their breakage: this happens at the distance of about $7d_i$ from the particle
 578 entrance in an RCS for electron beams and at the distances about $12d_i$ for proton beams, where d_i is
 579 the ion inertial depth. This demonstrated that in some locations of current sheet the turbulence can be
 580 generated by accelerated electron beams, while in others by proton beams. In addition, there is electron-ion
 581 hybrid instability, the kinetic branch of Kelvin-Helmholtz instability, which can also enhancing the plasma

582 turbulence near the lower-hybrid frequency since there are clearly detected flows of proton/ions travelling
583 from the X-nullpoint to the O-nullpoint, This was consistent with the previous numerical findings for
584 simulations in different reconnecting regimes (Drake et al., 2003; Muñoz & Büchner, 2016) and the
585 observations in the Earth's magnetotail (Khotyaintsev et al., 2010).

586 In order to explore the kinetic turbulence in more detail, we distinguish the parallel and perpendicular
587 components of the electric and magnetic turbulent fields (Boldyrev et al., 2013; Loureiro & Boldyrev,
588 2017) that reveals different level of turbulence in the presence of a strong magnetic field. By analysing
589 the changes in the electric and magnetic fields in frequency domain at different locations, we can connect
590 non-Maxwellian features in the particle phase space with distinct fluctuations of turbulence. This frequency
591 analysis of the generated turbulence was carried inside the simulated current sheets: close to X-nullpoint
592 (point C), far away from X-nullpoint (point B) and inside O-nullpoint (point A). The frequency analysis
593 was also supported by Morlet wavelet analysis carried in the point B over the timescale of $80 \Omega_{ci}^{-1}$.

594 The particle distributions in the points A-C clearly demonstrate non-Maxwellian features in particle
595 distributions, e.g. the electron beam distribution in the location B in Fig. 7(c): at $z = 15d_i$ (or $\Delta z \sim 7d_i$
596 away from the main X-nullpoint) reveal two beams at the distance $x \sim 1.5$: one with lower velocities and
597 another one moving with much higher velocities while revealing a clear fragmented structure. In addition,
598 there are electron holes formed in the phase space between $x = -1.5d_i$ to $1.5d_i$, which can be triggered by
599 the beam-driven lower hybrid instability. Also we show that in the point A inside the magnetic island there
600 are a few proton beams observed with arc-type structure and a break in the flow that can also produce a
601 well defined turbulence.

602 The electron beams introduced high-frequency electromagnetic fluctuations above Ω_{ce} , which were
603 observed in Fig. 9 in the frequency spectra of the turbulence generated by beams in the surveyed points
604 (B-C) shown in Fig. 7 and also confirmed by the two wide purple strips below and above the electron
605 plasma frequency seen clearly in the wavelet spectra in Fig.8) calculated in the point B.

606 These rapid signals appear as distinct spikes near the high-frequency tail of the power spectra of electric
607 and magnetic fields in Fig. 9. These fluctuations are spread from the electron gyro frequency to the electron
608 plasma frequency. This high-frequency turbulence is likely to be generated by two-beam (Buneman), or
609 two-beam instability, of electron beams with 'bump-in-tail' distributions in the vicinity of X-nullpoint as
610 indicated by some other simulations (Siversky & Zharkova, 2009; Muñoz & Büchner, 2018) producing
611 Langmuir waves. Although, as one can observe from Fig. 7c, in some locations electron beams start
612 moving across the magnetic field lines producing the enhanced ultra-high frequency fluctuations in the
613 E_{\perp} component, or Bernstein waves (Bernstein, 1958; Guskov & Surkov, 2007). The similar signals were
614 found in the inflow region close to the X-nullpoint by Lapenta et al. (2020).

615 Such high-frequency harmonics above Ω_{ce} have been recently discovered by the MMS satellites near
616 the electron diffusion region in the magnetopause (Dokgo et al., 2019). On the other hand, Li et al. (2020)
617 reported the signals in E_{\perp} and B_{\perp} power spectra peak at the harmonics of $n\Omega_{ce}$, where $n = 1, 2, 3, \dots$ near
618 an electron diffusion region in the magnetotail and they were attributed to the electron Bernstein waves. One
619 difference in the observation is that $\omega_{pe}/\Omega_{ce} \approx 27$ in the magnetosphere, which keeps those two signals
620 well separated. But this ratio is much lower in most the PIC simulations including ours ($\omega_{pe}/\Omega_{ce} = 15$), so
621 we could not distinguish them clearly.

622 While in the location A deeper into the magnetic island there is seen perturbation in the ion phase space
623 at $z = 10d_i$ (or $\Delta z \sim 12d_i$ away from the X-nullpoint) in Fig. 7(b), with the three quasi-parallel arcs
624 located in the region between $x = 0$ to $2d_i$ and a very bright blob of very energetic protons located at $x = 0$

625 representing the different groups of the ion beams formed during acceleration. These few arcs are found to
626 disappear quickly further in the downstream of the beam that suggest the ion beams become scattered by
627 the plasma turbulence. Thus, the ion beams would also be quickly suppressed by two-stream instabilities.
628 The difference between the electron and ion phase space suggests that to understand the full picture of
629 plasma turbulence due to magnetic reconnection, it requires the simulation size to be much bigger than the
630 diffusion region (Eastwood et al., 2018; Zhang et al., 2019).

631 Although, there is a noticeable increase of the turbulence close to the lower-hybrid frequency in the
632 parallel components at the point A and in the perpendicular components in the points A and B (see Fig. 9
633 see parallel B in left top plot and perpendicular electric field E in the right bottom plot). As shown in the
634 lower plots of Fig. 7, the particle densities in these points A and B have well recorded inhomogeneities
635 of particle densities clearly seen in Fig. 7b,c. The lower-hybrid waves can be generated by two-stream
636 instabilities as shown in the energy distribution of Fig. 7b (Papadopoulos & Palmadesso, 1976; Fujimoto &
637 Sydora, 2008; Zhou et al., 2014; Xia & Zharkova, 2020), or due to the strong density gradient near the
638 separatrixes and in the outflow (Drake et al., 2003; Scholer et al., 2003; Divin et al., 2015; Zudin et al.,
639 2019).

640 In the current simulation the lower-hybrid waves are clearly seen in the both frequency and wavelet
641 analysis applied to the gathered kinetic turbulence. The wavelet power spectrum showed that the low-
642 frequency fluctuations at the lower-hybrid frequency dominate the region have largest amplitudes. These
643 turbulent electro-magnetic field enhancements near $f \approx \omega_{lh}$, $f < \Omega_{ce}$, and $\Omega_{ce} < f < \omega_{pe}$ are well
644 consistent with the bright yellow and red stripes in the wavelet power spectrum shown in section 3.3.1.

645 The field-aligned drifts often drive instabilities (Drake et al., 2003) revealing a growth of parallel
646 propagating turbulence initially and strong levels of oblique lower hybrid waves at later times coinciding
647 with substantial parallel electron acceleration (Fujimoto & Sydora, 2008). In low- β plasmas with intense
648 parallel currents and both with or without parallel E fields, LH waves are shown to grow even for electron
649 distributions stable to the parallel Buneman instability and to accelerate electrons parallel to B very rapidly
650 (McMillan & Cairns, 2006). This instability may be seen as the oblique limit of the ion acoustic and
651 Buneman instabilities (McMillan & Cairns, 2007). The low-frequency waves in the current model dominate
652 the turbulence in the regions located further away from the X-nullpoint (points A and B) since accelerated
653 particle beams become more intense (Fujimoto & Sydora, 2008) and amplitudes of the fluctuations are
654 increased near the lower-hybrid frequency (Rogers et al., 2000).

655 This suggestion is also consistent with the other study (McMillan & Cairns, 2007) showing that in
656 plasmas with low beta the most unstable mode is not occurring at parallel propagation, but may be at
657 intermediate and very oblique angles that is observed in the perpendicular components of turbulence in
658 the locations A and B shown in Fig. 9. Evidently, by splitting the electromagnetic fluctuations into the
659 parallel and perpendicular direction, we managed to identify the differences between these striped signals,
660 confirming them to be the real features since the oblique whistler waves are sometimes observed in thin
661 current sheets (Zhou et al., 2009; Artemyev et al., 2016).

662 Although, further investigation is required of the kinetic turbulence generated in reconnecting current
663 sheets with different magnetic field topologies and scenarios of reconnections and their links to the
664 specific acceleration paths of the ambient particles dragged into a current sheet with a given magnetic field
665 topology. This dual approach to investigation of kinetic turbulence combining investigation of accelerated
666 particle paths and distributions with the turbulence they can generate can help to uncover more accurately

667 the mechanisms for generation of kinetic turbulence during a magnetic reconnections and its effect on
668 accelerated particles and the whole reconnection process.

669 In summary, we have identified the plasma turbulence in the RCS with magnetic islands and linked
670 the characteristic fluctuations to the non-Maxwellian distributions of particles in the phase and frequency
671 spaces. The observed waves are found to vary as a function of the distance away from the X-nullpoint.
672 The high-frequency perpendicular fluctuations damp quickly out of the electron diffusion region, while
673 the lower-frequency lower-hybrid (possibly whistler) waves are developing because of the streaming
674 instabilities generated by two electron or two proton beams.

675 Identifying these characteristic signals in the observation could indicate the existing scenarios of local
676 particle acceleration during their passage through magnetic reconnection regions in the solar wind. These
677 results can be potentially beneficial for the in-situ observations of RCSs near the Sun obtained with the
678 Parker Solar Probe, which has already detected some reconnection sites during its first encounter (Phan
679 et al., 2020).

CONFLICT OF INTEREST STATEMENT

680 The authors declare that the research was conducted in the absence of any commercial or financial
681 relationships that could be construed as a potential conflict of interest.

FUNDING

682 The authors acknowledge the funding for this research provided by the U.S. Air Force grant *PRJ02156*.

ACKNOWLEDGMENTS

683 The authors wish to express their gratitude to the anonymous reviewers for their useful and constructive
684 comments from which the paper strongly benefited. The authors acknowledge the funding for this
685 research provided by the U.S. Air Force grant *PRJ02156*. This research used the DiRAC Complexity
686 system, operated by the University of Leicester IT Services, which forms part of the STFC DiRAC
687 HPC Facility (www.dirac.ac.uk). This equipment is funded by BIS National E-Infrastructure capital
688 grant ST/K000373/1 and STFC DiRAC Operations grant ST/K0003259/1. DiRAC is part of the National
689 e-Infrastructure.

REFERENCES

- 690 Angelopoulos, V., McFadden, J. P., Larson, D., et al. 2008, *Science*, 321, 931
691 Antiochos, S. K. 1998, *Astrophysical Journal, Letters*, 502, L181
692 Antiochos, S. K., Dahlburg, R. B., & Klimchuk, J. A. 1994, *Astrophysical Journal, Letters*, 420, L41
693 Artemyev, A., Agapitov, O., Mourenas, D., et al. 2016, *Space Science Review*, 200, 261
694 Arzner, K., & Scholer, M. 2001, *Journal of Geophysics Research*, 106, 3827
695 Bárta, M., Büchner, J., Karlický, M., & Skála, J. 2011, *Astrophysical Journal*, 737, 24
696 Benz, A. O. 2017, *Living Reviews in Solar Physics*, 14, 2
697 Bernstein, I. B. 1958, *Physical Review*, 109, 10
698 Bhattacharjee, A., Huang, Y.-M., Yang, H., & Rogers, B. 2009, *Physics of Plasmas*, 16, 112102
699 Birdsall, C. K., & Langdon, A. B. 1991, *Plasma Physics via Computer Simulation* (Adam Hilger, Bristol,
700 England)

- 701 Biskamp, D. 1986, in *Magnetic Reconnection and Turbulence*, ed. M. A. Dubois, D. Grésellon, & M. N.
702 Bussac, 19
- 703 Boldyrev, S., Horaites, K., Xia, Q., & Perez, J. C. 2013, *Astrophysical Journal*, 777, 41
- 704 Bowers, K. J., Albright, B. J., Yin, L., Bergen, B., & Kwan, T. J. T. 2008, *Physics of Plasmas*, 15, 055703
- 705 Buneman, O. 1958, *Phys. Rev. Lett.*, 1, 8
- 706 Burch, J. L., Moore, T. E., Torbert, R. B., & Giles, B. L. 2016, *Space Science Review*, 199, 5
- 707 Carter, T. A., Ji, H., Trintchouk, F., Yamada, M., & Kulsrud, R. M. 2002, *Physical Review Letters*, 88,
708 015001
- 709 Cattell, C., Dombeck, J., Wygant, J., et al. 2005, *Journal of Geophysical Research: Space Physics*, 110,
710 <https://agupubs.onlinelibrary.wiley.com/doi/pdf/10.1029/2004JA010519>
- 711 Cerutti, B., Werner, G. R., Uzdensky, D. A., & Begelman, M. C. 2013, *Astrophysical Journal*, 770, 147
- 712 —. 2014, *Astrophysical Journal*, 782, 104
- 713 Chen, L.-J., Bhattacharjee, A., Puhl-Quinn, P. A., et al. 2008, *Nature Physics*, 4, 19
- 714 Dahlin, J. T., Drake, J. F., & Swisdak, M. 2017, *Physics of Plasmas*, 24, 092110
- 715 Dalla, S., & Browning, P. K. 2005, *Astronomy and Astrophysics*, 436, 1103
- 716 Daughton, W. 1999, *Physics of Plasmas*, 6, 1329
- 717 Daughton, W., Lapenta, G., & Ricci, P. 2004, *Physical Review Letters*, 93, 105004
- 718 Daughton, W., Roytershteyn, V., Karimabadi, H., et al. 2011, *Nature Physics*, 7, 539
- 719 Divin, A., Khotyaintsev, Y. V., Vaivads, A., et al. 2015, *Journal of Geophysical Research (Space Physics)*,
720 120, 2675
- 721 Dokgo, K., Hwang, K.-J., Burch, J. L., et al. 2019, *Geophysics Research Letters*, 46, 7873
- 722 Drake, J. F., Opher, M., Swisdak, M., & Chamoun, J. N. 2010, *Astrophysical Journal*, 709, 963
- 723 Drake, J. F., Swisdak, M., Cattell, C., et al. 2003, *Science*, 299, 873
- 724 Drake, J. F., Swisdak, M., Che, H., & Shay, M. A. 2006, *Nature*, 443, 553
- 725 Eastwood, J. P., Mistry, R., Phan, T. D., et al. 2018, *Geophysical Research Letters*, 45, 4569
- 726 Egedal, J., Daughton, W., & Le, A. 2012, *Nature Physics*, 8, 321
- 727 Farge, M. 1992, *Annual Review of Fluid Mechanics*, 24, 395
- 728 Fletcher, L., Dennis, B. R., Hudson, H. S., et al. 2011, *Space Science Review*, 159, 19
- 729 Franci, L., Cerri, S. S., Califano, F., et al. 2017, *Astrophysical Journal, Letters*, 850, L16
- 730 Fujimoto, K. 2006, *Physics of Plasmas*, 13, 072904
- 731 —. 2014, *Geophysics Research Letters*, 41, 2721
- 732 Fujimoto, K., & Machida, S. 2006, *Journal of Geophysical Research (Space Physics)*, 111, A09216
- 733 Fujimoto, K., & Sydora, R. D. 2008, *Geophysics Research Letters*, 35, L19112
- 734 Furth, H. P., Killeen, J., & Rosenbluth, M. N. 1963, *Physics of Fluids*, 6, 459
- 735 Goldreich, P., & Sridhar, S. 1995, *Astrophysical Journal*, 438, 763
- 736 Gomberoff, L., Gomberoff, K., & Brinca, A. L. 2002, *Journal of Geophysical Research (Space Physics)*,
737 107, 1123
- 738 Guo, F., Li, H., Daughton, W., & Liu, Y.-H. 2014, *Physical Review Letters*, 113, 155005
- 739 Gusakov, E. Z., & Surkov, A. V. 2007, *Plasma Physics and Controlled Fusion*, 49, 631
- 740 Hesse, M., Kuznetsova, M., & Birn, J. 2001, *Journal of Geophysics Research*, 106, 29831
- 741 Holman, G. D., Aschwanden, M. J., Aurass, H., et al. 2011, *Space Science Review*, 159, 107
- 742 Howes, G. G., Dorland, W., Cowley, S. C., et al. 2008, *Physical Review Letters*, 100, 065004
- 743 Huang, C., Lu, Q., Wang, R., et al. 2017, *The Astrophysical Journal*, 835, 245
- 744 Huang, S. Y., Sahraoui, F., Retino, A., et al. 2016, *Geophysical Research Letters*, 43, 7850
- 745 Huang, Y.-M., & Bhattacharjee, A. 2010, *Physics of Plasmas*, 17, 062104

- 746 Hurford, G. J., Krucker, S., Lin, R. P., et al. 2006, *Astrophysical Journal, Letters*, 644, L93
- 747 Hurford, G. J., Schwartz, R. A., Krucker, S., et al. 2003, *Astrophysical Journal, Letters*, 595, L77
- 748 Jaroschek, C. H., Treumann, R. A., Lesch, H., & Scholer, M. 2004, *Physics of Plasmas*, 11, 1151
- 749 Karimabadi, H., Dorelli, J., Roytershteyn, V., Daughton, W., & Chacón, L. 2011, *Physical Review Letters*, 107, 025002
- 751 Karlický, M. 2008, *Astrophysical Journal*, 674, 1211
- 752 Khabarova, O., Zank, G. P., Li, G., et al. 2015, *Astrophysical Journal*, 808, 181
- 753 Khabarova, O., Zharkova, V., Xia, Q., & Malandraki, O. E. 2020, *The Astrophysical Journal*, 894, L12
- 754 Khabarova, O., Malandraki, O., Malova, H., et al. 2021, *Space Science Review*, 217, 38
- 755 Khabarova, O. V., Zank, G. P., Malandraki, O. E., et al. 2017, *Sun and Geosphere*, 12, 23
- 756 Khotyaintsev, Y. V., Vaivads, A., André, M., et al. 2010, *Phys. Rev. Lett.*, 105, 165002
- 757 Kucharek, H., Scholder, M., & Matthews, A. P. 2000, *Nonlinear Processes in Geophysics*, 7, 167
- 758 Lapenta, G. 2008, *Physical Review Letters*, 100, 235001
- 759 Lapenta, G., & Brackbill, J. U. 1997, *Journal of Geophysics Research*, 102, 27099
- 760 Lapenta, G., Markidis, S., Divin, A., Goldman, M. V., & Newman, D. L. 2011, *Geophysics Research Letters*, 38, L17104
- 762 Lapenta, G., Pucci, F., Goldman, M. V., & Newman, D. L. 2020, *Astrophysical Journal*, 888, 104
- 763 Le, A., Egedal, J., Ohia, O., et al. 2013, *Phys. Rev. Lett.*, 110, 135004
- 764 Li, W. Y., Graham, D. B., Khotyaintsev, Y. V., et al. 2020, *Nature Communications*, 11, 141
- 765 Li, X., Guo, F., Li, H., Stanier, A., & Kilian, P. 2019, *Astrophysical Journal*, 884, 118
- 766 Lin, J., Ko, Y.-K., Sui, L., et al. 2005, *Astrophysical Journal*, 622, 1251
- 767 Lin, R. P., Krucker, S., Hurford, G. J., et al. 2003, *Astrophysical Journal, Letters*, 595, L69
- 768 Litvinenko, Y. E. 1996, *Astrophysical Journal*, 462, 997
- 769 Litvinenko, Y. E., & Somov, B. V. 1993, *Solar Physics*, 146, 127
- 770 Loureiro, N. F., & Boldyrev, S. 2017, *Astrophysical Journal*, 850, 182
- 771 Loureiro, N. F., Cowley, S. C., Dorland, W. D., Haines, M. G., & Schekochihin, A. A. 2005, *Physical Review Letters*, 95, 235003
- 773 Loureiro, N. F., Schekochihin, A. A., & Cowley, S. C. 2007, *Physics of Plasmas*, 14, 100703
- 774 Markidis, S., Lapenta, G., Divin, A., et al. 2012, *Physics of Plasmas*, 19, 032119
- 775 Matthaeus, W. H., & Velli, M. 2011, *Space Science Review*, 160, 145
- 776 McMillan, B. F., & Cairns, I. H. 2006, *Physics of Plasmas*, 13, 052104
- 777 —. 2007, *Physics of Plasmas*, 14, 012103
- 778 Muñoz, P. A., & Büchner, J. 2016, *Physics of Plasmas*, 23, 102103
- 779 —. 2018, *Physical Review E*, 98, 043205
- 780 Nishizuka, N., Karlický, M., Janvier, M., & Bárta, M. 2015, *Astrophysical Journal*, 799, 126
- 781 Øieroset, M., Lin, R. P., Phan, T. D., Larson, D. E., & Bale, S. D. 2002, *Phys. Rev. Lett.*, 89, 195001
- 782 Øieroset, M., Phan, T. D., Fujimoto, M., Lin, R. P., & Lepping, R. P. 2001, *Nature*, 412, 414
- 783 Oka, M., Phan, T.-D., Krucker, S., Fujimoto, M., & Shinohara, I. 2010, *Astrophysical Journal*, 714, 915
- 784 Omura, Y., Matsumoto, H., Miyake, T., & Kojima, H. 1996, *Journal of Geophysics Research*, 101, 2685
- 785 Papadopoulos, K., & Palmadesso, P. 1976, *The Physics of Fluids*, 19, 605
- 786 Papini, E., Franci, L., Landi, S., et al. 2019, *Astrophysical Journal*, 870, 52
- 787 Pezzi, O., Liang, H., Juno, J. L., et al. 2021, *arXiv e-prints*, arXiv:2101.00722
- 788 Phan, T. D., Bale, S. D., Eastwood, J. P., et al. 2020, *Astrophysical Journal, Supplement*, 246, 34
- 789 Pritchett, P. L. 2005, *Physics of Plasmas*, 12, 062301
- 790 Pritchett, P. L., & Coroniti, F. V. 2004, *Journal of Geophysical Research (Space Physics)*, 109, A01220

- 791 Pucci, F., Servidio, S., Sorriso-Valvo, L., et al. 2017, *Astrophysical Journal*, 841, 60
792 Rogers, B. N., Drake, J. F., & Shay, M. A. 2000, *Geophysics Research Letters*, 27, 3157
793 Roytershteyn, V., Daughton, W., Karimabadi, H., & Mozer, F. S. 2012, *Phys. Rev. Lett.*, 108, 185001
794 Scholer, M., Sidorenko, I., Jaroschek, C. H., Treumann, R. A., & Zeiler, A. 2003, *Physics of Plasmas*, 10,
795 3521
796 Shay, M. A., Phan, T. D., Haggerty, C. C., et al. 2016, *Geophysical Research Letters*, 43, 4145
797 Silin, I., & Büchner, J. 2006, *Advances in Space Research*, 37, 1354
798 Sironi, L., & Spitkovsky, A. 2014, *Astrophysical Journal, Letters*, 783, L21
799 Siversky, T. V., & Zharkova, V. V. 2009, *Journal of Plasma Physics*, 75, 619
800 Song, H.-Q., Chen, Y., Li, G., Kong, X.-L., & Feng, S.-W. 2012, *Physical Review X*, 2, 021015
801 Takasao, S., Asai, A., Isobe, H., & Shibata, K. 2012, *Astrophysical Journal, Letters*, 745, L6
802 Trotta, D., Franci, L., Burgess, D., & Hellinger, P. 2020, *Astrophysical Journal*, 894, 136
803 Verboncoeur, J. P., Langdon, A. B., & Gladd, N. T. 1995, *Computer Physics Communications*, 87, 199
804 Vilmer, N., MacKinnon, A. L., & Hurford, G. J. 2011, *Space Science Review*, 159, 167
805 Wang, R., Lu, Q., Nakamura, R., et al. 2016, *Nature Physics*, 12, 263
806 Wood, P., & Neukirch, T. 2005, *Solar Phys.*, 226, 73
807 Xia, Q., & Zharkova, V. 2018, *Astronomy and Astrophysics*, 620, A121
808 —. 2020, *Astronomy and Astrophysics*, 635, A116
809 Zank, G. P., le Roux, J. A., Webb, G. M., Dosch, A., & Khabarova, O. 2014, *Astrophysical Journal*, 797, 28
810 Zenitani, S., & Hoshino, M. 2008, *Astrophysical Journal*, 677, 530
811 Zhang, Q., Drake, J. F., & Swisdak, M. 2019, *Physics of Plasmas*, 26, 102115
812 Zharkova, V., & Agapitov, O. V. 2009, *Journal of Plasma Physics*, 75, 159
813 Zharkova, V., & Gordovskyy, M. 2004, *Astrophysical Journal*, 604, 884
814 —. 2005, *MNRAS*, 356, 1107
815 Zharkova, V., & Khabarova, O. 2015, *Annales Geophysicae*, 33, 457
816 Zharkova, V., & Khabarova, O. V. 2012, *Astrophysical Journal*, 752, 35
817 Zharkova, V., Arzner, K., Benz, A. O., et al. 2011, *Space Science Review*, 159, 357
818 Zhong, J. Y., Lin, J., Li, Y. T., et al. 2016, *The Astrophysical Journal Supplement Series*, 225, 30
819 Zhou, M., Li, H., Deng, X., et al. 2014, *Journal of Geophysical Research: Space Physics*, 119, 8228
820 Zhou, M., Deng, X. H., Li, S. Y., et al. 2009, *Journal of Geophysics Research*, 114, A02216
821 Zong, Q.-G., Fritz, T. A., Pu, Z. Y., et al. 2004, *Geophysics Research Letters*, 31, L18803
822 Zudin, I. Y., Zaboronkova, T. M., Gushchin, M. E., et al. 2019, *Journal of Geophysical Research (Space*
823 *Physics)*, 124, 4739